The Global Navigation Satellite System (GNSS): Positioning, Velocities, and Reflections

Ronni Grapenthin

Abstract Since the inception and realization of the Global Positioning System (GPS) in the 1970-1980s, the Global Satellite Navigation System (GNSS) has become a ubiquous tool in civil, business, and scientific life. Major breakthroughs in our understanding of dynamic Earth processes were only achievable through this precise positioning technology. While positioning is the chief objective of the system, the nature of its design requires satellite signals to traverse the ionosphere and the troposphere, and results in signal reflections off the ground. In addition to crustal dynamics, this enables the study of the atmosphere and local environmental sensing, impacting fields far beyond solid earth research, including space physics, atmospheric science, glaciology, hydrology, and natural hazards.

In this paper I review some of the history of this technology and its impact on the Earth sciences. Using the example of GPS, I introduce how satellite positioning systems work and how we can infer precise positions from the signals broadcast by the satellites. For this, I give an overview on reference systems, different observation models, the predominant precise positioning strategies and how the various error terms can be corrected. Once a solid understanding of precise positioning is developed, I present some of the complications that arise in high-rate (1 or more sample per second observations) sub-daily and real-time kinematic positioning, which is of great utility in the characterization and monitoring of many natural hazards.

GNSS enables observations beyond precise positioning. I provide background and observation models for instantaneous velocity estimations, useful in real-time applications particularly where precise orbits and intial positions are not available, and GNSS reflectometry, which allows to perform local environmental sensing around GNSS monuments, including the inference of snow depth or tidal heights.

Throughout the paper, each method is illustrated by a number of applications either from the literature or novel work. The focus is on some highlights from the last

Ronni Grapenthin

Geophysical Institute, University of Alaska Fairbanks, 2156 Koyukuk Dr., Fairbanks, AK-99775, USA, e-mail: rgrapenthin@alaska.edu

decade of geodetic work, with a clear slant towards examples from solid Earth and hydrologic research.

1 Introduction

After more than 20 years of development (e.g., *Easton*, 1974) and conceptual testing by the U.S. Department of Defense, the Global Positioning System (GPS) achieved full constellation in 1993. The system, in which satellites broadcast civil and military signals modulated onto sinusoidal carrier signals, lends itself to many uses in Earth science spanning solid earth geophysics, surface processes, atmospheric science and space weather. The ability to achieve millimeter positioning precision by tracking the carrier phase (e.g., *Counselman et al.*, 1980; *Counselman and Gourevitch*, 1981; *Hoffmann-Wellenhof et al.*, 2008; *Misra and Enge*, 2011) in addition to utilizing the much less precise ranging codes nothing less but revolutionized the field.

GPS enabled direct measurements of plate motions (e.g., *Feigl et al.*, 1993) on a global scale at an affordable cost per receiver (e.g., *Segall and Davis*, 1997). Since then, polar motion measurements improved with GNSS (e.g., *Herring et al.*, 1991; *Desai and Sibois*, 2016), tectonic plate motion velocity models are being refined (e.g., *Argus and Heflin*, 1995; *Argus et al.*, 2010), micro-plates (e.g., *Jansma et al.*, 2000; *Wallace et al.*, 2004; *Apel et al.*, 2006) and terranes (e.g., *Fletcher and Freymueller*, 1999; *Elliott et al.*, 2010) have been identified or characterized, further constraining terrestrial dynamics (*Copley et al.*, 2011) and informing on seismic hazards (e.g., *Newman*, 1999; *Bilham et al.*, 2001). In addition to capturing deformation during earthquake ruptures (e.g., *Grapenthin and Freymueller*, 2011), and mapping the recorded surface deformation back to slip on finite fault surfaces (e.g., *Simons et al.*, 2011; *Galetzka et al.*, 2015), another important contribution to seismic hazard assessment arising from GNSS observations is the recording of plate boundary processes such as interseismic strain buildup (e.g. *Wang*, 2001, Figure 1), slow slip (e.g., *Dragert et al.*, 2001; *Rogers and Dragert*, 2003), and the amount of coupling between the subducting and overriding plates (e.g., *Freymueller et al.*, 2008).

Near volcanoes, we can resolve subsurface magma migration (e.g., *Cervelli et al.*, 2006; *Elsworth et al.*, 2008; *Hreinsdóttir et al.*, 2014), co-eruptive magma extrusion driven deformation (e.g., *Sigmundsson et al.*, 2015), and even piston-like motion due to caldera collapse (*Gudmundsson et al.*, 2016; *Neal et al.*, 2019). Beyond tectonic and magmatic applications, we capture crustal deformation due to dynamics of the cryosphere and hydrosphere (e.g., *Heki*, 2001; *Grapenthin et al.*, 2006; *Amos et al.*, 2014; *Borsa et al.*, 2014; *Argus et al.*, 2014), including the resolution of hemispheric mass exchange due to seasonal winter loading of the continents (*Blewitt et al.*, 2001).

Subdaily (e.g., *Nikolaidis et al.*, 2001), high-rate (e.g., *Larson et al.*, 2003; *Galetzka et al.*, 2015), and real-time GNSS (e.g., *Grapenthin et al.*, 2014b; *Melgar et al.*, 2019; *Melbourne et al.*, 2019) applications in geophysics have been developed over the last two decades. The major limitation to enable this technology, particularly
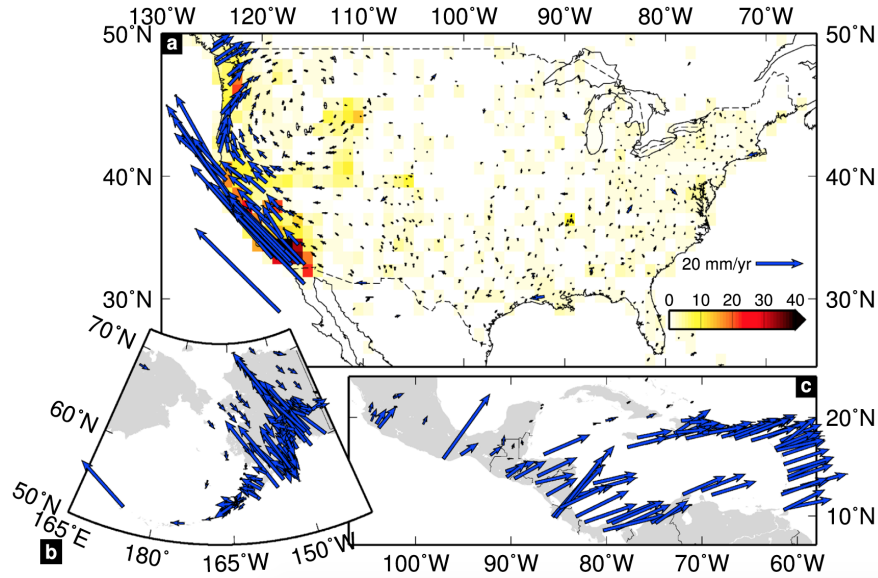
Fig. 1 Horizontal velocity solutions from *Herring et al.* (2016) for the Network of the Americas (NOTA) spanning the contiguous US (a), Alaska (b) and the Caribbean (c). Uncertainties at the 95% confidence level are plotted at the arrow tips, but are not visible at this scale. West of 100° W only about 15% of the available stations are shown, the background color in panel (a) indicates the 1°x1° station density. Source: *Herring et al.* (2016)

in the geophysically most interesting, remote locations, is the design of sustainable power supply and telemetry systems that support the transfer of the large data volumes resulting from high-rate (1 sps) to very high-rate (up to 50 sps) observations. In regions where the engineering challenges can be met, GNSS can be used in real-time hazard analysis (e.g., *Grapenthin et al.*, 2014b; *Melgar et al.*, 2019) and early warning (e.g., *Murray et al.*, 2018) as was successfully demonstrated for the 2014 M_w 6.0 South Napa earthquake in California (*Grapenthin et al.*, 2014a) and the 2019 M_w 7.1 Ridgecrest earthquake (*Melgar et al.*, 2019), also in California. However, real-time GPS-only positioning precision is at the centimeter-level, even when using high-quality dual-frequency receivers. The lower magnitude threshold for GNSS to resolve any meaningful depends very much on the distance from the hypocenter. For crustal faults with nearby GNSS stations, recording of events in the M 5 range is possible (e.g., *Geng et al.*, 2013).

A recent development lowering the position noise has been the combination of accelerometers and high-rate GNSS positions to generate seismogeodetic data streams that provide positions at accelerometer frequencies (*Bock et al.*, 2011). This requires collocation of accelerometers at geodetic-quality GNSS stations and resolves earthquake displacements at the temporal resolution of the accelerometer. The technique depends on the alignment of positioning solutions from GNSS and accelerometer data, which are downweighted in the combination to suppress accelerometer drift.

The propagation of the satellite signal through the ionosphere, the troposphere, and its reflection off the ground before reaching the antenna resulted in the development of several non-positioning applications that use GNSS as a remote sensing tool. For instance, GNSS is used to characterize total electron content of the ionosphere (e.g., *Mannucci et al.*, 1998), resulting in applications to not only monitor space weather, but also propagation of accoustic and gravity waves due to earthquakes (e.g., *Calais and Minster*, 1995), volcanic eruptions (e.g., *Heki*, 2006), explosions (e.g., *Fitzgerald*, 1997) and tsunamis (e.g., *Artru et al.*, 2005). *Meng et al.* (2019) provide an excellent, more extensive overview of theory and measurement techniques of upper atmosphere perturbations. GNSS can furthermore be used to characterize the distribution of precipitable water content in the troposphere (e.g., *Bevis et al.*, 1992); detect and characterize volcanic ash plumes (e.g., *Houlié et al.*, 2005; *Grapenthin et al.*, 2013; *Larson*, 2013; *Grapenthin et al.*, 2018a); and to determine local snow depth, soil moisture, vegetation water content, or decadal changes of permafrost around the GNSS monument (e.g., *Larson*, 2016, 2019; *Liu and Larson*, 2018). At coastal sites, ocean tides (*Larson et al.*, 2013) and storm surges (*Peng et al.*, 2019) have been estimated, turning GNSS into a tide gauge that can be decoupled from surface deformation and is registered in a global reference frame. This astonishing richness in applications of a single observation system can be explained through the observation models described below.

Several other satellite positioning constellations have been developed and established, such as the European Galileo, the Russian GLONASS, and the Chinese BeiDou, which are all globally operating, while the Indian NAVIC and the Japanese QZSS operate regionally (see *Hoffmann-Wellenhof et al.*, 2008; *Misra and Enge*, 2011, for details). Combined, these constellations form the Global Navigation Satellite System (GNSS). Multi-GNSS analysis approaches can use a large number of signals from these different systems and promise significant noise reduction for both classic static analysis and kinematic or real-time applications (e.g., *Geng et al.*, 2018). Effective positioning estimation approaches leveraging the strength of all available signals are still a very active area of research (e.g., *Montenbruck et al.*, 2014; *Liu et al.*, 2017; *Geng et al.*, 2019; *Zheng et al.*, 2019). For the purposes of this paper, however, we will focus on the legacy GPS constellation that transmits on two frequencies L1 (1575.42 MHz) and L2 (1227.60 MHz).

2 How GNSS works

The GPS constellation requires a minimum of 24 satellites, orbiting the earth at 20,350 km. The satellites are distributed on 6 orbital planes that are inclined at 55 degrees (Figure 2). This design results in repeated ground tracks for each GPS satellite at about 11 hour 58 minute periods (see *Agnew and Larson*, 2006, for more precise repeat time calculations). While 24 satellites are required to guarantee a minimum of 4 visible satellites, more satellites are in orbit to strengthen the constellation and add redundancy (30 operational satellites on 09 October 2019,

https://www.navcen.uscg.gov/). Monitoring of satellite health, orbits, and other tasks to maintain the system are performed by system of ground stations that are globally distributed such that each satellite is always in view of at least two ground stations.

Fig. 2 GPS constellation model. The minimum constellation requires 4 satellites on each of the 6 orbital planes (grey lines) that are inclined 55 degrees to each other. *Source: GPS.gov*
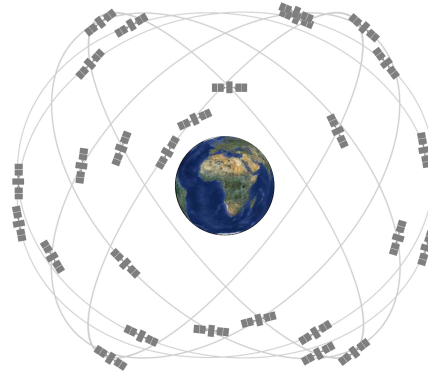
The GPS satellites broadcast signals on at least two radio frequencies: Link 1 (L1, 1575.42 MHz) and Link 2 (L2, 1227.60 MHz). The carrier signals at these frequencies are derived from a 10.23 MHz atomic clock on board of the satellites. Legacy GPS provides just one signal on L1, the coarse/acquisition (C/A) signal, to be used for several-meter precision civil positioning applications. However, phase tracking of the carrier signals on L1 and L2 enables the very precise (mm-precision for static applications) uses of GPS. As operational GPS satellites near their end-of-life, they are replaced with newer generations, offering opportunities to modernize the system. New demands on navigation and interoperability with other systems, and general advances in technology result in the addition of new signals and even new transmission bands. Notable is L2C, a new civilian, unencrypted signal that is currently available on 19 satellites and has a higher signal-to-noise ratio than the C/A signal. Operational status for L2C (availablility on 24 GPS satellites) is currently expected for 2021 (https://www.gps.gov/systems/gps/modernization/civilsignals/). The availability of two unencrypted civilian signals will enable the mitigation of ionospheric delay without the need to track and resolve ambiguities for the carrier phase (see below), which will bring a significant improvement of consumer positioning applications as dual frequency receivers become more affordable. Additionally, twelve satellites also broadcast on L5 (1176.45 MHz), a dedicated safety-of-life signal in a protected frequency band (unlike L2), which will provide an additional civilian-use signal at higher power, which is expected to be operational in 2024. Two civilian signals in a protected frequency band (L1 C/A, and L5) will enable robust precision navigation (due to ionospheric delay mitigation) for aircraft and other sensitive equipment requiring high position precision.

3 Positioning in a Nutshell

The main applications of GNSS relate to positioning and position changes, and the provision of precise global timing. The advance that came with the availability of precise timing is that positioning could move from the measurement of angles to the measurement of distances. GNSS works by determining the distance between receiver and satellites and then solving for the position that puts the receiver where the various distances from all tracked satellites intersect. One of the satellites, though, will be used to correct the much less precise clock of the ground receiver. These four unknowns (latitude, longitude, height, time) require as least four satellites in view, which became the main design criterion for the GPS constellation. However, because GNSS signals traverse the ionosphere and troposphere, and are reflected off of the ground and interfere with signals arriving directly at the antenna from the satellites, precise positioning requires treatment of these error terms. Here, I will first introduce reference systems used in GNSS analysis, after which I will present the observation models that link satellite observations to the desired estimates for position and time. Following this, I will discuss the treatment of the error terms to further enhance the position precision.

3.1 Reference Systems

Two Cartesian coordinate systems are necessary to realize GNSS positioning. Both are well-defined, which allows transformations of points in one reference system to the other (see, e.g., *Hoffmann-Wellenhof et al.*, 2008). The first coordinate system is Earth-centered space-fixed, which is necessary to express satellite motions around a sun-orbiting Earth. The origin is defined at Earth's center of mass, the z-axis corresponds to the average direction of Earth's rotation axis (Celestial Intermediate Pole, CIP), the x-axis points to the vernal equinox in an equitorial plane and the y-axis is selected to make the coordinate system right-handed (e.g., *Misra and Enge*, 2011). Varying speeds around the sun as well as precession and nutation of the axis of rotation pose potential issues in defining a stable coordinate system, but these processes are well understood and can be embedded in the realization of the reference system.

The second, and for our purposes more prominent coordinate system, is Earth-centered Earth-fixed (ECEF). It rotates with the Earth, which means the user position is fixed. While it has a formal definition, it is realized through a set of points and their velocities to account for tectonic plate motion (*Bock and Melgar*, 2016). One such time-variable realization of a reference frame is the World Geodetic System 1984 (WGS84, *Decker*, 1986), common to consumer-grade GPS applications and maintained by the US National Geospatial Agency. Another reference system, the International Terrestrial Reference Frame (ITRF) is updated more frequently as extended time series at ground stations allow for increased precision, analysis approaches improve, and more stations globally allow for tighter constraints on the

reference frame. The most recent version is ITRF14 (*Altamimi et al.*, 2016), which for the first time also includes non-linear station motions induced by annual seasonal variations and post-seismic deformation at sites near large earthquakes (*Altamimi et al.*, 2016).

As Cartesian coordinates are not very intuitive to convey a position and its change on the Earth's surface, we can define a smooth reference model in the form of an ellipsoid, with the same origin as the ECEF system. The z-axis is the axis of revolution of the ellipsoid and, for instance, WGS84 defines the ellipsoid semi-major axis and its flattening. Once the ellipsoid is defined, we can transform from $[X, Y, Z]$ coordinates to latitude, longitude and height on the ellipsoid (e.g., *Hoffmann-Wellenhof et al.*, 2008; *Bock and Melgar*, 2016).

At this point it is crucial to understand that the absolute height values for GNSS are given above a reference ellipsoid (as defined by, e.g., WGS84). This is a smooth oblate simplification of the Earth's shape. Traditionally, however, height values have been given with respect to mean sea level which is expressed through the geoid (e.g., Earth Gravitational Model 2008 (EGM2008), *Pavlis et al.*, 2012). This is an undulating equipotential surface that varies with the position-dependent gravitational potential of the Earth. Differences between reference ellipsoid and geoid can be tens of meters. Hence, it is important to note the reference frame in which heights are given, particularly when comparisons to topographic heights are made, which are generally with respect to mean sea level.

Once we build up time series of GNSS positions at a single site, we are generally interested in change over time. This change is more intuitive when position solutions $[X_i, Y_i, Z_i]$ at epoch i relative to an initial position $[X_0, Y_0, Z_0]$ at epoch 0 are rotated into a local North-East-Up (NEU) system (e.g., *Bock and Melgar*, 2016):

$$\begin{bmatrix} \Delta N_i \\ \Delta E_i \\ \Delta U_i \end{bmatrix} = \begin{bmatrix} -sin(\phi)\,cos(\lambda) & -sin(\lambda)) & sin(\phi)\,cos(\phi) \\ -sin(\lambda) & cos(\lambda) & 0 \\ cos(\lambda)\,cos(\phi) & cos(\phi)\,sin(\lambda) & sin(\phi) \end{bmatrix} \begin{bmatrix} X_i - X_0 \\ Y_i - Y_0 \\ Z_i - Z_0 \end{bmatrix} \qquad (1)$$

where ϕ and λ are the geodetic latitude and longitude of the site, respectively.

The dominant signal (in the horizontal component) of GNSS time series is generally the steady-state rigid tectonic plate motion. Removal of this signal is often desired to highlight short-term transients or unmodeled temporal signals, for instance interseismic strain buildup along the plate boundaries (Figure 1). Plate velocities are determined from geodetic observations at locations of the continent that are presumed stable and are expressed as angular velocity around an Euler Pole, which represents a translation on a sphere. Recent global plate velocity models are, for instance, GEODVEL by *Argus et al.* (2010) or the model by *Kreemer et al.* (2014). North America-centric ones such as NA12 (*Blewitt et al.*, 2013) or NAM14 (*Herring et al.*, 2016) are also available.

3.2 Pseudorange Model

With the importance of reference frames to positioning addressed, we can move toward the mathematical models behind GNSS positioning. The **range** describes the geometric distance between two points, in our case a satellite and a receiver. This could, for instance, be inferred by measuring the transit time, τ, of a signal that travels from satellite to receiver at the speed of light, c, if the signal contains a timestamp for the send time an the receiver notes the arrival time. However, the GNSS receiver has an imprecise clock, and the signal travel path is affected by path delay effects due to ionosphere and troposphere and other error sources, resulting in longer travel than the pure geometric distance would suggest. Hence, we call the range observable provided by a GNSS receiver a **pseudorange** to a satellite.

The pseudorange from receiver u to satellite s, $\rho^{(s)}$ (in length units), can be expressed as a superposition of the true geometric range $r^{(s)}$ to satellite s and the known error sources (*Misra and Enge*, 2011):

$$\rho^{(s)} = r^{(s)} + c(\delta t_u - \delta t^{(s)}) + I + T + \epsilon \tag{2}$$

where c remains the speed of light, δt_u is the receiver clock bias, $\delta t^{(s)}$ is clock bias of satellite s (the broadcast ephimeris typically results in accuracy to a few meters; more precise products are available or special processing strategies can remove this error term; see below) and I, T are ionospheric and tropospheric delays. The last term, ϵ, captures unmodeled effects, such as multipath, measurement errors, etc. (see Section 3.4). Note that subscripts (e.g., u) reflect receiver specific values, while superscripts identify individual satellites; these are not powers of (s)!

Substituting the geometric range between satellite and receiver in earth-centered-earth-fixed Cartesian coordinates into Equation 2 and linearizing the result via Taylor series expansion about an approximate initial position and expected receiver clock bias (x_0, y_0, z_0, t_{e_0}), in vector notation we get:

$$\Delta\rho^{(s)} = \left[\begin{array}{cccc} \frac{\partial\rho^{(s)}}{\partial x} & \frac{\partial\rho^{(s)}}{\partial y} & \frac{\partial\rho^{(s)}}{\partial z} & \frac{\partial\rho^{(s)}}{\partial t_e} \end{array} \right] \begin{bmatrix} \Delta x \\ \Delta y \\ \Delta z \\ \Delta t_e \end{bmatrix} + \epsilon \tag{3}$$

Here $\Delta\rho^{(s)}$ is the difference between the measured pseudorange (observed by the receiver) and the expected geometric range between the satellite position and the apriori position. The terms $[\Delta x, \Delta y, \Delta z, \Delta t_e]$ are the difference between the actual receiver position and the initial approximation. Adding these values to the approximated position will yield an improved absolute position estimate. To simplify Equation 3, all error terms are absorbed into ϵ for the time being.

If we solve the partial derivatives in Equation 3 by applying the chain rule and appropriate substitutions, we are left with:

$$\Delta\rho^{(s)} = \left[\begin{array}{cccc} \frac{x_0-x^{(s)}}{\rho_0^{(s)}} & \frac{y_0-y^{(s)}}{\rho_0^{(s)}} & \frac{z_0-z^{(s)}}{\rho_0^{(s)}} & c \end{array} \right] \begin{bmatrix} \Delta x \\ \Delta y \\ \Delta z \\ \Delta t_e \end{bmatrix} + \epsilon \tag{4}$$

where the $(x^{(s)}, y^{(s)}, z^{(s)})$ remains the position of satellite s and $\rho_0^{(s)}$ is the approximated distance between the receiver's approximated initial position and satellite s, whose position we assume to be known here. Assuming that we have n satellites in view, each of which giving us a pseudorange measurement $\rho^{(1)}, \ldots, \rho^{(n)}$, we can set up a linear system of equations in matrix-vector notation:

$$\begin{bmatrix} \Delta\rho^{(1)} \\ \Delta\rho^{(2)} \\ \vdots \\ \Delta\rho^{(n)} \end{bmatrix} = \begin{bmatrix} \frac{x_0-x^{(1)}}{\rho_0^{(1)}} & \frac{y_0-y^{(1)}}{\rho_0^{(1)}} & \frac{z_0-z^{(1)}}{\rho_0^{(1)}} & c \\ \frac{x_0-x^{(2)}}{\rho_0^{(2)}} & \frac{y_0-y^{(2)}}{\rho_0^{(2)}} & \frac{z_0-z^{(2)}}{\rho_0^{(2)}} & c \\ \vdots & \vdots & \vdots & \vdots \\ \frac{x_0-x^{(n)}}{\rho_0^{(n)}} & \frac{y_0-y^{(n)}}{\rho_0^{(n)}} & \frac{z_0-z^{(n)}}{\rho_0^{(n)}} & c \end{bmatrix} \begin{bmatrix} \Delta x \\ \Delta y \\ \Delta z \\ \Delta t_e \end{bmatrix} + \epsilon \tag{5}$$

$$d = Gm + \epsilon \tag{6}$$

Equation 6 represents a shorthand of Equation 5 where G contains the partial derivatives, d is a vector holding the pseudorange differences and m is a vector of unknown differences between actual and approximate position and receiver clock error. Given G and d, we can solve this linear system of equations for m with least squares techniques (e.g., for general least squares solutions see *Aster et al.*, 2018; *Lichten*, 1989, is a reference for GNSS specific analyses) to minimize the sum of squared residuals, for instance, using the normal equations:

$$m = (G^T G)^{-1} G^T d \tag{7}$$

We could also introduce a weight matrix W to, for instance, reduce the impact of satellites at low elevation angles on the solution as they provide noisier signals due to longer signal paths through Earth's atmosphere:

$$m = (G^T W G)^{-1} G^T W d \tag{8}$$

where W can be diagonal and contains, for instance, the reciprocal variances of the measurements $\frac{1}{\sigma^2}$. Using the inverse of the full data covariance matrix as weight matrix W is a more rigorous approach as this also accounts for correlations between the measurements in space and time (e.g., *Bock and Melgar*, 2016).

Once we have a solution $m = [\Delta x, \Delta y, \Delta z, \Delta t_e]$ we can add it to the apriori values to get an updated absolute position:

$$\begin{bmatrix} x_{new} \\ y_{new} \\ z_{new} \\ t_{e_{new}} \end{bmatrix} = \begin{bmatrix} x_0 \\ y_0 \\ z_0 \\ t_{e_0} \end{bmatrix} + \begin{bmatrix} \Delta x \\ \Delta y \\ \Delta z \\ \Delta t_e \end{bmatrix} \tag{9}$$

and iterate until improvements are small.

3.3 Carrier Phase Model and Ambiguity Resolution

A more precise measure of a receiver position can be achieved by tracking the carrier phase of the signal. *Misra and Enge* (2011) describe in detail several methods of how a receiver tracks the carrier phase, the details of which are beyond the scope of this paper. Assuming, we have measurements of the phase observable in units of cycles, the observation model equation for satellite s is (*Misra and Enge*, 2011):

$$\Phi^s = \lambda^{-1}[r^{(s)} + I_{\Phi}^{(s)} + T_{\Phi}^{(s)}] + f(\delta t_u - \delta t^{(s)}) + N^{(s)} + \epsilon_{\Phi} \tag{10}$$

where λ is the carrier signal wavelength and f is the carrier frequency ($f = c/\lambda$, where c is the speed of light), r remains the geometric range between satellite and receiver and I_{Φ} and T_{Φ} are the ionospheric and tropospheric propagation delays, respectively. The clock errors are again captured by δt_u and δt^s for receiver and satellite clocks, respectively. An important new term in this model is N^s, the integer ambiguity for satellite s.

The solution strategy for finding the geometric range between satellite and receiver remains similar to that in Section 3.2 above. However, before this can be done, we need to find the correct value for N, the integer ambiguity. This term represents the number of cycles that the signal has gone through before the receiver started tracking the signal. One can imagine that when the satellite first appears on the horizon, the receiver captures the factional phase of the signal and keeps adding or removing full cycles as it maintains lock to the satellite. Given the sinusoidal nature of the carrier signal the total number of cycles required to travel from satellite to receiver is unknown. All we know is that it must be an integer number of cycles. Several strategies have been proposed to solve this problem, commonly captured under the term ambiguity resolution.

A number of approaches exist to resolve integer ambiguities. One instructive analytical method uses the dual frequency measurements of the phase on L1 and L2 and combines them into a wide-lane measurement, Φ_{12} (e.g., *Misra and Enge*, 2011):

$$\Phi_{12} = \Phi_1 - \Phi_2 = \frac{r}{\lambda_{12}} + N_{12} + \epsilon_{\Phi_{12}} \tag{11}$$

The resulting longer wavelength, $\lambda_{12} = c/(f_{L1} - f_{L2}) = 0.862$ m, of the combined signal reduces the uncertainty in the integer ambiguity estimate, but also amplifies the noise in the signal, which is the reason we do not use this combination for

positioning. N_{12} is the difference of the integer ambiguities on L1 and L2 and can be estimated as (e.g., *Misra and Enge*, 2011):

$$\hat{N}_{12} = \left[\Phi_{12} - \frac{\rho_1}{\lambda_{12}} \right]_{\text{roundoff}} \tag{12}$$

Misra and Enge (2011) determine that the standard deviation of this estimate is about 1.2 cycles, suggesting that this could be reduced to less that 0.5 cycle with uncorrelated measurements over 10 epochs, and even more with additional measurements. Once we have an acceptable estimate for the widelane integer ambiguity, we can use this to estimate the L1 and L2 integer ambiguities by solving the (simplified) measurement models for the range (e.g., *Misra and Enge*, 2011):

$$r = \lambda_1(\Phi_1 - N_1 - \epsilon_{\Phi_1})$$
$$r = \lambda_2(\Phi_2 - N_2 - \epsilon_{\Phi_2})$$

and equating them:

$$\lambda_1(\Phi_1 - N_1 - \epsilon_{\Phi_1}) = \lambda_2(\Phi_2 - N_2 - \epsilon_{\Phi_2}) \tag{13}$$

$$N_1 - \frac{\lambda_2}{\lambda_1}N_2 = \Phi_1\frac{\lambda_2}{\lambda_1}\Phi_2 + \epsilon \tag{14}$$

Since $N_1 - N_2 = N_{12}$, we can solve Equation 14 to estimate N_1 and N_2 (e.g. *Misra and Enge*, 2011):

$$\hat{N}_1 = \left[1 - \frac{\lambda_2}{\lambda_1} \right]^{-1} \left[\Phi_1 - \frac{\lambda_2}{\lambda_1}\Phi_2 - \frac{\lambda_2}{\lambda_1}N_{12} \right] \tag{15}$$

$$\hat{N}_2 = \left[1 + \frac{\lambda_2}{\lambda_1} \right]^{-1} \left[-\Phi_1 + \frac{\lambda_2}{\lambda_1}\Phi_2 + N_{12} \right] \tag{16}$$

Equations 15 and 16 have not been corrected for the impact of the ionosphere, however. The next section below will explore how to eliminate such nuisance terms. It should be obvious that this approach will benefit significantly from the upcoming triple frequency observations. However, ambiguity resolution through widelane estimation is by no means a guarantee as it relies on good data quality (*Misra and Enge*, 2011).

Following this analytical approach, I want to briefly discuss search solutions that resolve the integer ambiguities for all satellites simultaneously. *Hoffmann-Wellenhof et al.* (2008), *Misra and Enge* (2011), and *Bock and Melgar* (2016) discuss these methods at greater depth. Most prominent is the Least-squares AMBiguity Decorrelation Adjustment method (LAMBDA method, *Teunissen*, 1993, 1995). The basic principle of the LAMBDA algorithm is to first find a least-squares float positioning solution that disregards the integer property of the ambiguities and estimates floating

point ambiguities. The next step then decorrelates the ambiguities, and hence reduces the search space to allow for a mapping to integer values in the transformed space. Lastly, the integer ambiguity estimates are used to find a fixed positioning solution.

3.4 Precise Positioning Strategies and Error Terms

When introducing pseudorange and carrier phase positioning and the respective observation models (Equations 2, 10), we have neglected to address any of the error terms. If our goal is to achieve sub-centimeter positioning, we need to correct the delay introduced by the ionosphere, dry and wet delays imposed on the signal in the troposphere, and in some cases direct and indirect arrivals of the signal from the satellite at the receiver (so called multi-path, MP).

Treatment of these nuisance terms is intimately related to the data processing strategy used to determine the GNSS position. Below, I introduce the two dominant strategies: network processing (*Dong and Bock*, 1989; *Blewitt*, 1989) and precise point positioning (*Zumberge et al.*, 1997) and discuss how the nuisance terms are treated or eliminated. It is important to keep in mind that these terms complicate the positioning problem, but they can and have been exploited as signals to constrain the properties of the medium that the GNSS signals propagate through.

3.4.1 Differential or Network Processing

In differential positioning, observables from several stations and satellites are differenced to eliminate some of the nuisance parameters from the observation model. The simplest example is that of a signle station pair. If we difference the observations from one satellite recorded at these two stations, we can eliminate the satellite clock error. Differencing observations from two satellites at the same receiver eliminates the receiver clock error. Forming the double difference of these two results will eliminate both clock errors. For the carrier phase measurement from satellite k recorded at receivers u, and r we can write the two observation models and form the single difference (see Equation 10):

$$
\begin{aligned}
\phi_u^{(k)} &= \frac{1}{\lambda} * (r_u^{(k)} + I_u^{(k)} + T_u^{(k)}) + f * (\delta t_u - \delta t^{(k)}) + N_u^{(k)} + \epsilon_{\phi,u}^{(k)} \\
\phi_r^{(k)} &= \frac{1}{\lambda} * (r_r^{(k)} + I_r^{(k)} + T_r^{(k)}) + f * (\delta t_r - \delta t^{(k)}) + N_r^{(k)} + \epsilon_{\phi,r}^{(k)} \\
\phi_{ur}^{(k)} &= \phi_u^{(k)} - \phi_r^{(k)} \\
&= \frac{1}{\lambda} * (r_{ur}^{(k)} + I_{ur}^{(k)} + T_{ur}^{(k)}) + f * \delta t_{ur} + N_{ur}^{(k)} + \epsilon_{\phi,ur}^{(k)} \qquad (17)
\end{aligned}
$$

Here, the satellite clock error, $\delta t^{(k)}$, is common to the observations and effectively cancels in the difference. If we make the assumption that the baseline is short, for example on the order of tens of kilometers, the ionosphere and troposphere errors may also be small as the signal likely traverses the same atmosphere to reach both stations. However, in many instances, significantly different local weather patterns may prohibit this assumption:

$$\phi_{ur}^{(k)} = \frac{r_{ur}^{(k)}}{\lambda} + f * \delta t_{ur} + N_{ur}^{(k)} + \epsilon_{\phi,ur}^{(k)} \tag{18}$$

If we form a similar single difference for the same receivers, u and r, but a different satellite, l, we get:

$$\begin{aligned}
\phi_{ur}^{(l)} &= \phi_u^{(l)} - \phi_r^{(l)} \\
&= \frac{r_{ur}^{(l)}}{\lambda} + f * \delta t_{ur} + N_{ur}^{(l)} + \epsilon_{\phi,ur}^{(l)}
\end{aligned} \tag{19}$$

We can now use Equations 18 and 19 to form the double difference and eliminate the receiver clock errors captured in δt_{ur}:

$$\begin{aligned}
\phi_{ur}^{(kl)} &= \phi_{ur}^{(k)} - \phi_{ur}^{(l)} \\
&= (\phi_u^{(k)} - \phi_r^{(k)}) - (\phi_u^{(l)} - \phi_r^{(l)}) \\
&= \frac{r_{ur}^{(kl)}}{\lambda} + N_{ur}^{(kl)} + \epsilon_{\phi,ur}^{(kl)}
\end{aligned} \tag{20}$$

At this stage, we are still left with the need to estimate at least the integer ambiguities. While the atmosphere and ionosphere may cancel in the single differences, we can treat them by applying models in precision position estimation. Common models for the atmosphere include the global pressure and temperature model and the global mapping function (GPT/GMF) (*Boehm et al.*, 2006a, 2007), the Vienna Mapping Function (*Boehm et al.*, 2006b, (VMF1)), or GPT2 (*Lagler et al.*, 2013). If no ionosphere-free linear combinations of the carrier phase observables are used (e.g., *Hoffmann-Wellenhof et al.*, 2008; *Misra and Enge*, 2011; *Bock and Melgar*, 2016), ionospheric corrections from NASA's Jet Propulsion Laboratory (JPL) or the International GNSS Service (IGS) can be applied. Furthermore, to achieve precice positioning solutions, solid earth tide and ocean tidal loading (OTL) effects, driven by the gravitional attraction of Sun and Moon, must be considered. As summarized by *Bock and Melgar* (2016), solid Earth tides can reach up to 1 m and the elastic response of the Earth to OTL can achieve 10 cm. While models applied in the processing can especially remove the solid Earth effects (e.g., International Earth Rotation and Reference Systems 2010 conventions *Gérard and Luzum*, 2011), great care must be taken when correcting for OTL as the coefficents (e.g., FES2004 *Lyard et al.*, 2006), must be inferred for the same reference system as orbit parameters if

estimated separately (e.g., center of mass of the solid Earth, CE versus center of mass of the Earth system CM *Fu et al.*, 2012), otherwise systematic errors will be introduced in the time series. *Herring et al.* (2016) provide a very detailed account of the specifics of the EarthScope Plate Boundary Observatory (PBO, *Silver et al.*, 1998) double-difference processing.

3.4.2 Precise Point Positioning

While the double difference approach works very well, the increasing number of available GNSS stations results in significant computational burden. Approaches to mediate this process smaller sized subnets individually and merge resulting solutions together (*Herring et al.*, 2016). This can be somewhat cumbersome.

A different strategy processes each station individually and is called precise point positioning, or PPP (*Zumberge et al.*, 1997). The immediately obvious drawback is that the satellite clock errors cannot be removed from the solution. Instead, this approach requires external products to provide these corrections. While these products require a network solution, the globally distributed network of stations can be much smaller than the number of stations we are usually generating positioning solutions for (*Zumberge et al.*, 1997). It is important that the models, including the antenna phase center models, used in the generation of the external products (such as clock corrections) are the same as the ones applied in the PPP positioning solutions or the result may include systematic position errors. Ionospheric and tropospheric delays, and solid Earth and ocean tides can be mediated through the same models described above for double differencing. *Herring et al.* (2016) describes in detail the PPP processing strategy for the EarthScope PBO network.

3.5 Applications

Figure 3 shows examples of daily station positioning solutions, here for stations P595 (*UNAVCO Community*, 2005b) and CCCC (*UNAVCO Community*, 2005a) in the Mojave Desert in California in a local NEU coordinate system. Each dot represents the position estimate for a single day, uncertainties are shown as gray bars. The solutions were generated by the National Science Foundation's Geodetic Facility for the Advancement of Geoscience (NSF-GAGE) facility as described by *Herring et al.* (2016). I removed very few large outliers. The time series have the rigid plate motion of the North American plate removed. The vertical component shows small seasonal effects that may be due to precipitation. The linear trends in the horizontal components are consistent with plate boundary processes. Over larger areas, these trends and their uncertainties are estimated and analyzed in the form of velocity maps (e.g., Figure 1) that show, for instance, large scale plate boundary processes. Notably, the linear trends in the horizontal compo-

nents terminate in two steps due to the July 2019 Ridgecrest earthquake sequence (https://earthquake.usgs.gov/earthquakes/eventpage/ci38457511/executive).
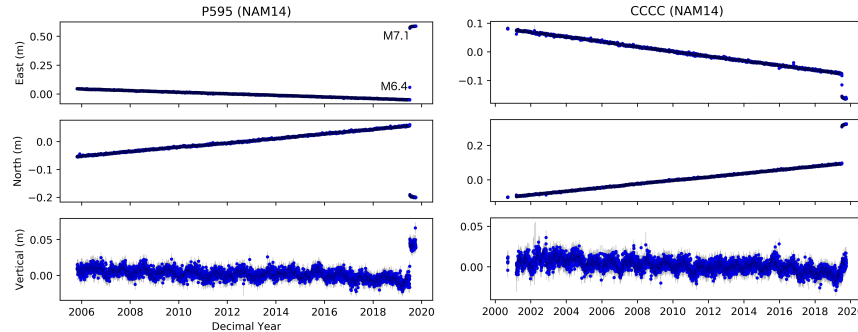

Fig. 3 GPS time series in east, north and vertical components for two stations in the Mojave desert in California. The time series are in a stable North America reference frame (NAM14, (*Herring et al.*, 2016)) The vertical components show slight seasonal deformation in annual cycles with time-varying amplitudes due to variable precipitation. The horizontal components show clear linear trends consistent with NNW motion caused by the transform plate boundary between the Pacific and the North American plates and resulting distributed deformation across the Eastern California Shear Zone. Two steps are marked and indicate offsets due to M_w 6.4 and M_w 7.1 earthquakes near the town of Ridgecrest on 04 and 06 July 2019. Data processed by NSF-GAGE facility as described by *Herring et al.* (2016).

It is clear from the figure that the time series are complex with multiple processes superimposed on each other. This is after the well-understood processes, such as earth and ocean tides, have been removed. Identification, analysis and modeling of these processes has furthered our understanding of Earth processes significantly over the last decades. With continuous time series now approaching, and in some instances exceeding, 20 years, much more subtle and longer term transient signals will be resolved. In Figure 3, for instance, both sites seem to show a subtle rate change in the vertical component over the last 3 years, when compared to the previous years. The seasonal variations in the vertical components show well, even for these desert sites, that precipitation from 2012-2014 was low compared to other years.

The recognition that seasonal signals in continuous GPS time series are linked precipitation came about in the early 2000s. *Heki* (2001) first connected the seasonal sinusoids in the GPS observations of the dense, continuous GEONET in Japan to the substantial snow loading in the mountains, which induces winter subsidence and summer uplift of the elastic crust. With the establishment of broad and dense continuout GNSS instrumentation in the Western United States through the PBO network similar observations of seasonal loading and inference of the respective water equivalent snow loads have been made there (e.g., *Fu and Freymueller*, 2012; *Argus et al.*, 2014; *Fu et al.*, 2015). Figure 4 shows a longer term application of these new hydrogeodetic observations as *Borsa et al.* (2014) visualize the drought evolution in the Western U.S. with the vertical displacements from March 2011 to

March 2014. At the beginning of spring we would expect wide spread subsidence due to snow loading as observed in 2011. However, starting in 2012 and very clear in 2013 and 2014, the GNSS sites recorded increasing uplift consistent with lacking precipitation. This uplift is particularly evident in the Sierra Nevada and Costal Ranges of California, for which *Amos et al.* (2014) also showed long-term uplift due to substantial long-term ground water extraction in the San Joaqin Valley (southern part of gray patch in Figure 4).
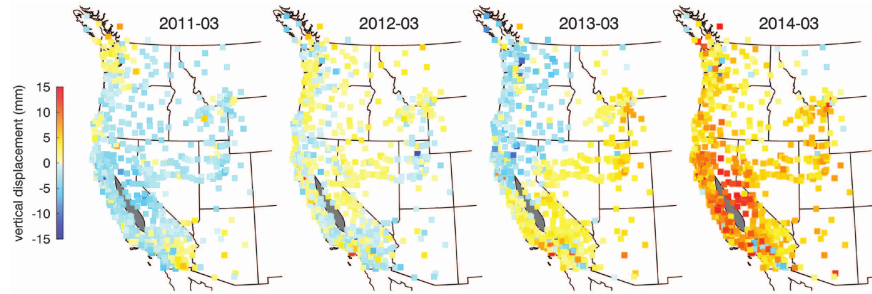
Fig. 4 Vertical GNSS displacements across the Western United States from March 2011 to March 2014. Squares mark GNSS station locations with colors indicated recorded vertical displacements. The gray patch shows the location of California's Central Valley where stations were excluded as they move in the opposite directions due to soil compaction during water extraction. From: *Borsa et al.* (2014).

4 High-rate and Real-time Positioning

All of our discussion so far has focused on static positioning: finding the most precise position of a station for a given day of data. Because of the high precision, time series of subsequent static solutions can reveal subtle, months-long processes such as magma recharge into a volcanic edifice that induces less than 2 cm of deformation (e.g., *Dixon et al.*, 1997; *Cervelli et al.*, 2006; *Fournier et al.*, 2009; *Grapenthin et al.*, 2013). However, many processes, such as earthquakes or volcanic eruptions work on much shorter time scales and benefit from kinematic GNSS solutions on subdaily timescales. Here, we can broadly distinguish two main approaches (either work in network or PPP mode): post-processed epoch-by-epoch solutions and true real-time processing. Before explaining these, I have to touch on a peculiar pitfall that arises when converting between GPS and UTC times.

4.1 Leap Seconds

Something we could ignore so far, but have to pay close attention to now, is the fact that GPS time is running ahead of UTC time by a time-variable number of seconds. UTC time is adjusted to stay in tune with the Earth's general slowdown in rotation and rotational irregularities in order to keep it aligned with mean solar time at Greenwich. To that end, leap seconds are occasionally introduced to UTC, 27 seconds since its establishment in 1970. GPS time, introduced in 1980, was initially aligned with UTC time, but it does not have a requirement to align with Earth's rotations. Hence, no leap seconds were ever introduced to GPS time, which since January 2017 is now 18 seconds ahead of UTC time.

Why is this important? Most times, such as earthquake origin times (https://earthquake.usgs.gov/earthquakes/map/) are given as UTC times. If any meaningful comparison of GNSS signals and physical processes are desired, the two time systems need to be aligned. This is easily achieved by subtracting the correct number of leap seconds from the GPS time stamps. As leap seconds are introduced irregularly, this requires a look-up table.

## 4.2 Epoch-by-Epoch Postprocessing

The kinematic use case of position estimation for each epoch of observations under the assumption that the receiver is moving is not that different from the static use case and is, in fact, one of the main application areas for GNSS positioning. In geophysics, *Nikolaidis et al.* (2001) was among the first to show dynamic motion due to a seismic wave using 30 s observations of the 1999 M_w 7.1 Hector Mine earthquake. *Larson et al.* (2003) used 1 sps data to resolve dynamic motion induced by the 2002 M_w 7.9 Denali earthquake and *Galetzka et al.* (2015) resolved the dynamic slip propagation along the fault during the M_w 7.8 Gorkha earthquake from 5 sps data.

The main complication that arises here is positioning noise due to signal multipath (e.g., *Georgiadou and Kleusberg*, 1988, Figure 5) and the resulting interference of the direct and indirect signals at the antenna. This is a slowly varying process with periods from minutes to hours and amplitudes on the order of centimeters (*Georgiadou and Kleusberg*, 1988). For the GPS constellation, these errors repeat approximately every 11 hours and 58 minutes, which is one revolution period of the GPS satellites. Multipath is generally not modeled and removed directly for static positioning under the assumption that it averages out with the use of an entire day of data and this average signal is repetitive on subsequent days (sometimes low elevation satellite data are masked out in particularly bad multipath environments). For subdaily kinematic positioning, this assumption no longer holds and multipath should be treated if the signal of interest is of similar magnitude. Since antenna design cannot fully shield against surface reflected signals, several methods for multipath reduction exist. *Axelrad et al.* (1996), for instance propose a technique to correct multipath in double differenced phase observations. On a time series level, sidereal filtering is an effective technique where, for instance, low-pass filtered observations

Fig. 5 Multipath geometry where the ground is a reflector. Antenna height and satellite elevation angle (*e*) determine the additional path length of the reflected signal (red line) that result in time-varying interference with the direct signal (blue) measured by the GPS antennas. The inset shows interference examples. From: *Larson* (2016).
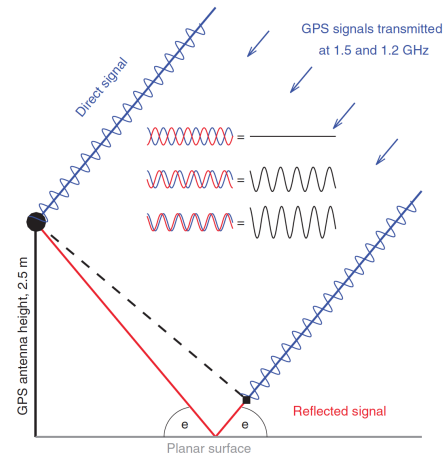
from the previous day (without a geophysical signal) are removed from the current day with the noisy signal (e.g., *Larson et al.*, 2007, Figure 6). However, for this to yield best results the use of the correct orbit repeat times is recommended to calculate the time shift before the signal subtraction (*Choi et al.*, 2004; *Agnew and Larson*, 2006) as the GPS constellation does not exactly repeat after 11 hours and 58 minutes (*Agnew and Larson*, 2006)
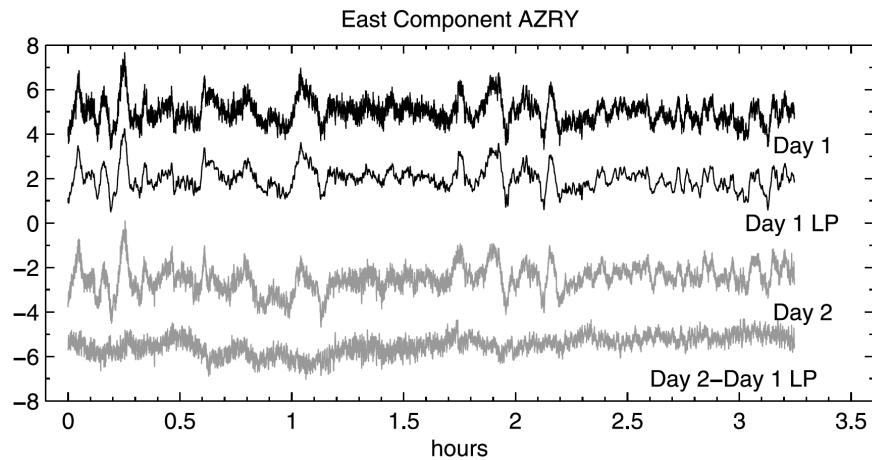
Fig. 6 Example of repeated noise due to multipath (Day 1 top trace, Day 2 third trace) in 1 Hz position data. Forward shifting of the Day 1 data by the average orbit repeat time and low pass filtering yields the Day 1 LP trace, which is subtracted from Day 2 to result in the fourth trace, a much cleaner time series. From: *Larson et al.* (2007).

4.3 Real-time Complications

Moving from the epoch-by-epoch postprocessing case to a real-time setting poses a few additional challenges. Obviously, a hardened telemetry system is required to deliver the data in a timely fashion with minimum data loss. This likely increases the power requirements, which poses additional engineering challenges at remote locations.

On a technical level, however, the main requirement for real-time processing is that it cannot fall behind the data delivery. This means, each epoch must be processed before the next arrives. This puts an upper limit on any iterative processes that run during position estimation, potentially reducing precision. Additionally, any smoothing of the time series will have to be limited due to time constraints. Further, for network processing, we are also somewhat limited by the number of sites that can be processed simultaneously as the computational time increases by N^3 (*Zumberge et al.*, 1997), where N is the number of stations. To avoid this while still benefiting from the elimination of nuisance terms through double-differencing, simple baseline processing has proven adequate for many applications. Here, a single roving station is processed relative to a base station that is assumed static. Since mathematically, this is equivalent to subtracting motion at the base station from the roving station, this relationship can be expressed in the mathematical models analyzing the positioning data, and absolute positioning may not be required. *Grapenthin et al.* (2014b) have demonstrated that this can be an effective real-time GNSS analysis strategy for earthquake early warning in a crustal fault setting and *Grapenthin et al.* (2014a) (see Section 4.4) captured and analyzed the 2014 $M_w6.0$ California Napa strike-slip earthquake this way in real-time. This strategy is applicable to many processes that induce local to regional deformation, such as landslide monitoring or volcanic deformation.

Large subduction zone earthquakes, on the other hand, could pose a significant challenge for such a differential processing strategy as short, and in particular trench parallel baselines may not resolve the translation of the entire network well enough above the noise (see Section 4.4). Hence, these events are best dealt with using a PPP processing scheme. Just like before, in the static positioning case, this poses additional challenges as the satellite clock errors need to be corrected. Troposphere and ionosphere delays also require dedicated treatment to achieve positioning precision to centimeter levels. Real-time orbit information and clock corrections are now distributed by the IGS to allow for PPP positioning in real-time (http://rts.igs.org). Commonly these products are provided in 30 s resolution, which we can interpolate due to the generally smooth nature of the variations. Commercial solutions are available, too. Trimble, for instance, broadcasts globally its own corrections and performs PPP positioning on site for its receivers to stream centimeter-level positioning solutions from the field (Trimble RTX). Real-time processing of a global network of stations may allow the dedicated user to generate their own corrections, too. As these clock corrections are calculated and distributed in real-time, delays in the range of 10-20 s are to be expected for the IGS real time service (e.g., *Hadas and Bosy*,

2015). Instantenous velocity-derived displacements (see Section 5) may be able to bridge this latency gap.

During our work on the real-time GNSS integration into an earthquake early warning syste, (*Grapenthin et al.*, 2014b), Ingrid Johanson (USGS-HVO) suggested an experiment to test the real-time processing system with large antenna offsets. We set up 7 tripods on the roof of McCone Hall, the building housing the Berkley Seismological Laboratory and the Department of Earth and Planetary Science, on the University of California Berkeley campus (Figure 7a). Four tripods had antennas mounted and connected to GPS receivers. One setup served as base station (BASE), the other three were supposed to experience a rapid large offset. We carried the antennas to the remaining three tripods that were 1, 3, and 6 meters away from the initial location (Figure 7a). We collected data for an hour, ducked below the ground plane of the antenna and quickly carried it to the receiving tripod to collect data for another hour. The processing was based on trackRT, the real time component of GAMIT/GLOBK (*Herring et al.*, 2010), with parameter settings similar to the real time network running at the time (*Grapenthin et al.*, 2014b). The generated displacements for each station were relative to the static base station BASE.

The experiment yielded the key insight that real-time processing should not be optimized to static observations. As the motion of the kinematic GPS stations is modeled as a random walk, a key parameter is the process noise that constrains how much random walk noise is assumed for a time step. Figure 7b shows a comparison between post-processed "true" displacements (top), and low processing noise (middle) and high process noise (bottom) real-time displacement time series for the 6 m offset experiment. It is obvious that too tightly constrained process noise results in a prolonged ramp rather than a near instantaneous step function. Notable remains the "overshoot" in the high process noise time series (Figure 7b, bottom). This is due to the identification and insertion of cycle-slips for all satellites at the time of the offsets by the processing software. Figure 7c shows the results for all three offsets with high process noise and (one from) of cycle slip detection suppressed. While some satellites are still flagged with a cycle slip, enough remain to produce a well constrained solution and clean step function matching the post-processed time series.

4.4 Applications

In this section I present some recent examples to showcase the potential of high-rate and real-time GNSS solutions to characterize, for instance, earthquakes or volcanic eruptions.

First, I analyze 5 sps observations to generate kinematic time series for the M_w 7.8 Gorkha, Nepal, earthquake (*Galetzka et al.*, 2015). I use final IGS orbits and IGS08 antenna phase center models (*Dow et al.*, 2009), remove solid Earth and ocean tides, and to model the atmosphere, I use the GPT2 global pressure and temperature model (*Lagler et al.*, 2013). I estimate the kinematic position solution as a random walk process.
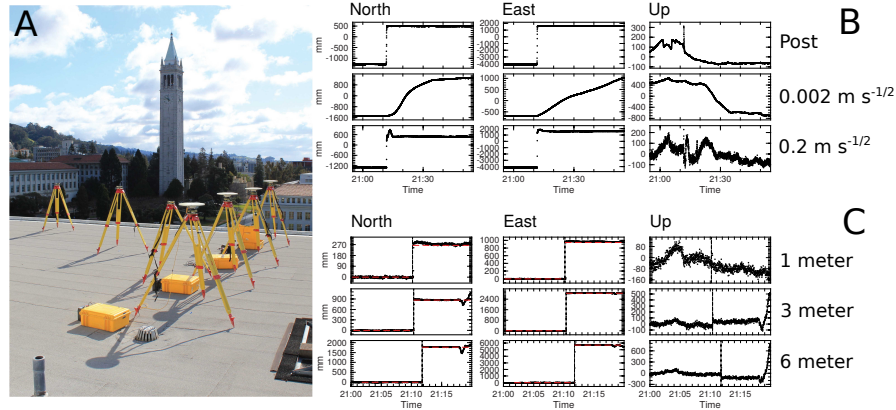
Fig. 7 (a) Experiment setup, tripods without antennas are 1, 3, and 6 meters from origin tripods, photo: R. Grapenthin. (b) Six-meter offset time series. Postprocessed on top, low process noise $(0.002\ m/\sqrt{s})$ in the middle, high process noise $(0.2\ m/\sqrt{s})$ at the bottom. (c) All three distances with high process noise and suppressed cycle slip detection. Time series courtesy of Ingrid Johanson, USGS-HVO.

The resulting time series for the two sites KKN4 and NAST are shown in Figure 8. The time series begin at the earthquake origin time (2015-04-25 06:11:25 (UTC)) and have properly taken into account that GPS time was 16 seconds ahead of UTC in 2015. The data show very clear the more than 20 seconds that it takes for the S-wave to travel from the hypocenter to these sites. NAST is also clearly further away from the hypocenter than KKN4 and shows much longer lasting dynamic excitation. This is due to its location within the Kathmandu basin, which traps and amplifies seismic energy (*Galetzka et al.*, 2015).

The very dense high-rate GNSS network of Japan captured the 2011 $M_w 9.0$ Tohoku-oki earthquake (*Simons et al.*, 2011). *Grapenthin and Freymueller* (2011) animated the timeseries for each station in map view to visualize the spatial propagation of the dynamic wavefield and the build-up of the static displacements in both horizontal and vertical components. Figure 9 shows a snapshot about 3 min 30 seconds after the origin time. The co-seismic static offsets have fully developed at this time and the S-wave and surface waves are traversing southern and northern Japan. Amazingly, these dynamic features can be highlighted if we subtract the final static offsets from the top row in Figure 9, which yields the bottom row.

The 2014 $M_6.0$ South Napa earthquake in California was the first earthquake captured and analyzed for slip distribution and magnitude in real-time (*Grapenthin et al.*, 2014a). Figure 10 shows a double difference solution for this event. All data, including the finite fault slip model, that went into this figure were in fact available 26 s after the event, as indicated in the figure. The first GNSS-based magnitude solution was available 24 s after the event. *Grapenthin et al.* (2014a) reported that a software error resulted in an artificial delay of the processing by 10 seconds. With 8 seconds S-wave travel time from the hypocenter to the nearest GNSS station and

## 5-Hz GNSS Displacements M7.8 Gorkha Earthquake
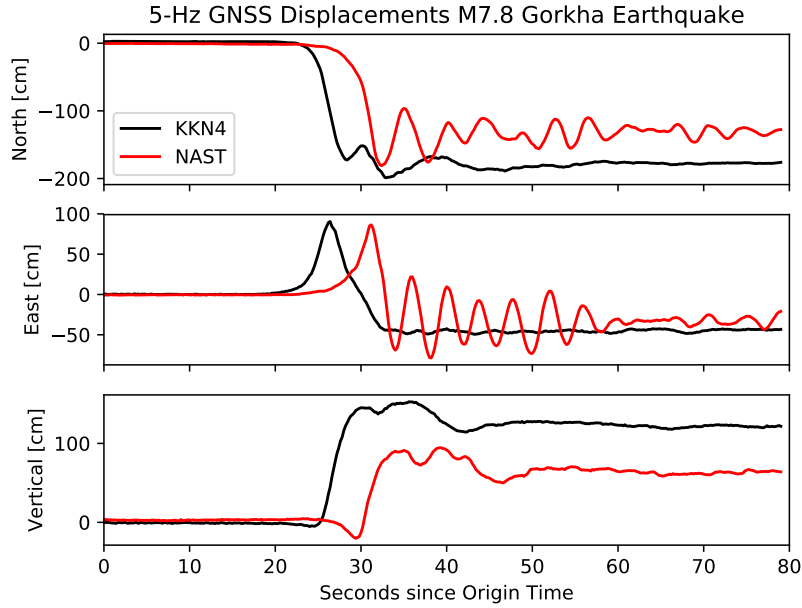
Fig. 8 Displacements at two GNSS sites during the 25 April 2019 Gorkha earthquake in Nepal (see Figure 12 for location). The sites clearly show different responses. KKN4 is located on bedrock, whereas NAST is located in the Katmandu Basin, which traps significant amounts of seismic energy, resulting in the long-term excitation at the site.

6 seconds data acquisition and processing latency, the map and model shown in Figure 10 could have been available after just 14 seconds.

More recently, the 2019 Ridgecrest earthquake sequence provided another test of the capabilities of real-time GNSS for rapid earthquake analysis and early-warning in a densely instrumented region. *Melgar et al.* (2019) perform a detailed comparison of archived real-time and postprocessed positioning solutions, concluding that the real-time GNSS performance during the Ridgecrest sequence manifested its utility as a monitoring and early warning tool. Hence, *Melbourne et al.* (2019) rightfully point out the significant potential of real-time GNSS to augment existing hazard monitoring tools.

A point in case is the 2018 Kīlauea eruption in Hawaii, my last example. *Neal et al.* (2019) present incredible GNSS time series, repoduced here in Figure 11, capturing the history of the caldera collapse at the summit. This is only rivaled by observations of about 65 m of GNSS-observed total subsidence at the caldera center during the 2015 Bardarbunga collapse (*Gudmundsson et al.*, 2016). Kīlauea GNSS stations NPIT and CALS provide a finely resolved history of collapse and broadening of the affected area. *Neal et al.* (2019) count 62 discrete collapse events, up to 8.5 m per event recorded at NPIT, resulting in a deepening of the caldera by more than 500 m
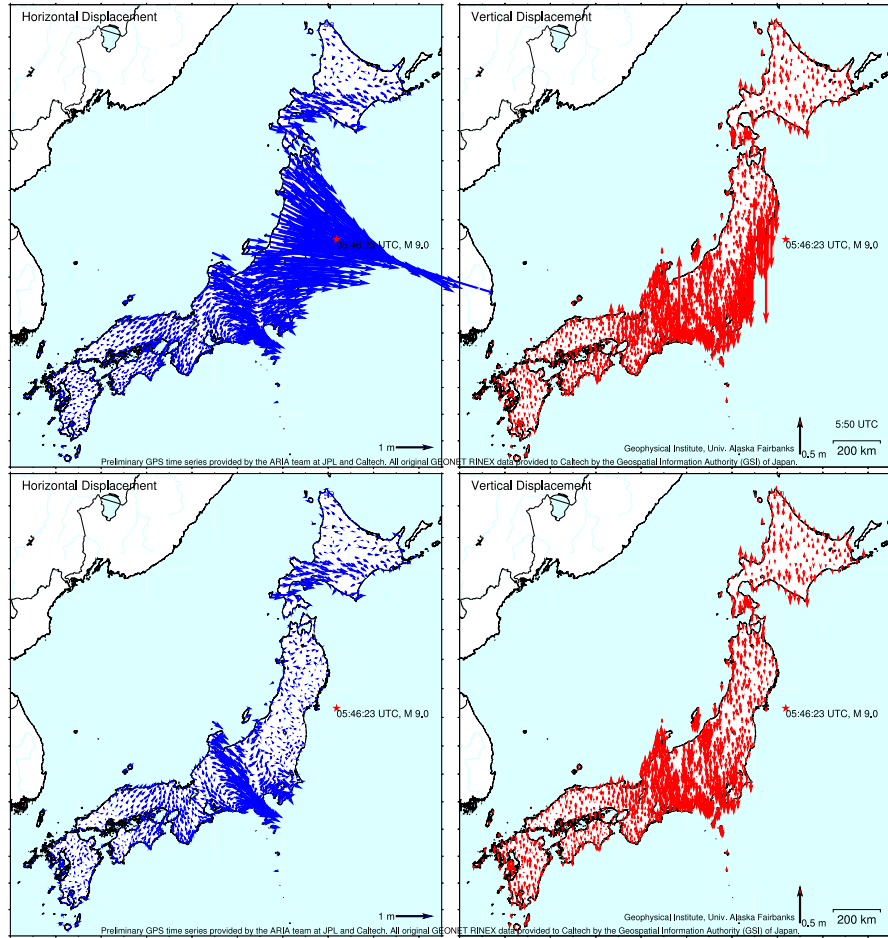
Fig. 9 The elastic wave field about 3:30 following the rupture initiation of the 11 March 2011 M_w 9.0 Tohoku-oki earthquake as sensed by about 1200 high-rate GNSS sites. The left panels show horizontal displacements, the right panels show vertical displacements. Lower row has the permanent co-seismic displacements subtracted to highlight the dynamic features. The S-wave packets are clearly visible in SE Japan in the horizontal panels, the Love-wave is slightly north of that. In the vertical panels we can see the Rayleigh wave (after *Grapenthin and Freymueller*, 2011).

in places. These observations contribute to a detailed model of onset of the caldera collapse (*Anderson et al.*, 2019) and the geometry of caldera bounding faults (*Segall et al.*, 2019), thus helping to understand the mechanics driving the collapse.
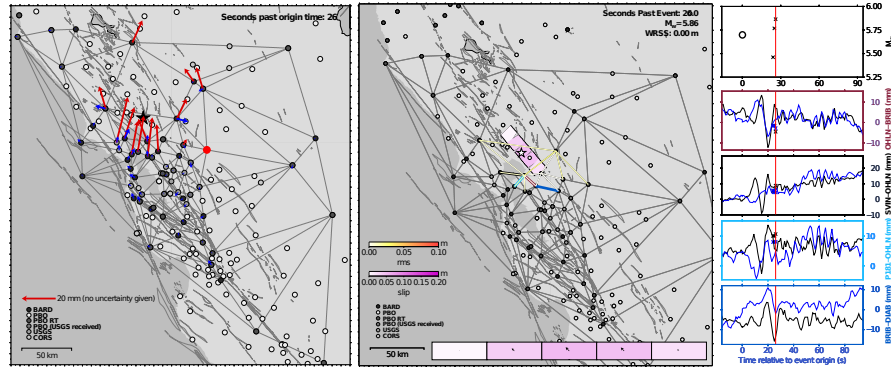
Fig. 10 2014 Napa earthquake real-time solution produced 26 s after origin time (event location given by star). The thin black lines (left, middle panels) indicate the network of baselines for which differential solutions were generated during this event. The left panel shows baseline offsets adjusted relative to site P256 (large red dot). The blue vectors are static horizontal offsets from rapid daily time series (courtesy of UNR). The red vectors indicate real-time offsets that are the difference between about 5 min of averaged preevent data and 3 s of averaged postevent data. The middle panel shows the finite slip model (vertical fault is rotated into map view) at 26 s after the event inferred from the red vector offsets in the left panel. White to yellow colored baselines indicate model resulting misfit to the data. Pink colors indicate slip amplitude. The right panel shows at the top the time series of GPS-inferred magnitude, the black circle indicates an initial seismic real-time estimate. The bottom four panels show north (blue) and east (black) displacement time series for the bold, similarly colored baselines in the middle panel. Crosses mark the offsets inferred along these baselines (time shift between GPS solutions and offsets is due to 6 s data acquisition and processing latency). From: *Grapenthin et al.* (2014a)

5 Instantaneous Velocities

A different approach to the use of both phase and range observables is to use the difference of subsequent measurements to infer instantaneous receiver velocities (e.g., *Grapenthin et al.*, 2018b), which is well known in geomatics (e.g., *Misra and Enge*, 2011; *Gaglione*, 2015). *Colosimo et al.* (2011) first applied this method to the geosciences and coined their algorithm VADASE (Variometric Approach for Displacement Analysis Stand-alone Engine), which they used to estimate earthquake waveforms and co-seismic displacements. As we will see below, this technique, when applied to carrier phase observations, works at surprisingly high precision even with just single frequency observations. This is due to the elimination of some of the error terms in the observation models (Equations 2 and 10). Assuming continuous tracking (i.e., no cycle slips), the constant integer ambiguity, N, is eliminated. If the observations are differenced over short time intervals, we can also neglect the effects of ionospheric and tropospheric delays, and solid Earth and ocean tides. Moreover, because of generally smooth satellite trajectories, we can use broadcast orbits to remove the satellite velocity from the observations and thus we are left with the receiver velocity as the primary product (e.g., *Misra and Enge*, 2011; *Grapenthin et al.*, 2018b). Here, we follow the derivation by *Grapenthin et al.* (2018b).
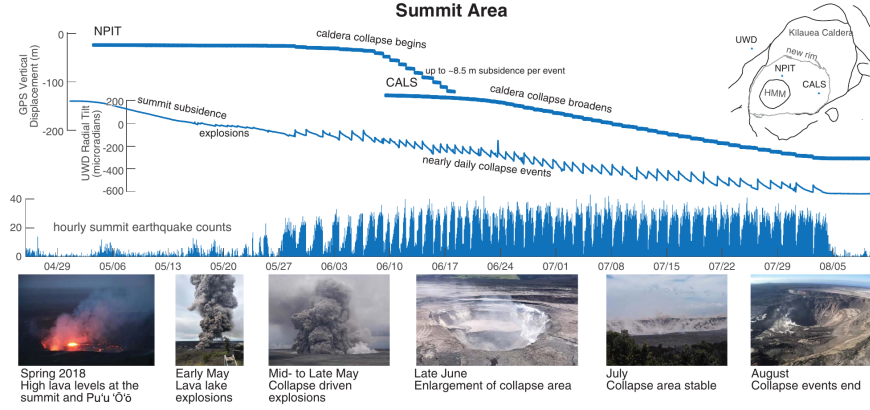
Fig. 11 Timeline of the activity Kīlauea's summit area during the 2018 eruption showing the GPS displacements at NPIT, CALS, radial tilt at UWD, hourly earthquake counts and representative pictures of the activity. The inset map shows station locations and caldera morphology, HMM marks Halemaʻumaʻu crater. NPIT is located close to the initial collapse focus and CALS is closer to the edge of the new rim, experienceing significant deformation later and in a less discrete, step-wise fashion. The tiltmeter spikes and spikes in earthquake counts show the near-daily collapse events. From: *Neal et al.* (2019)

5.1 Observation Model

An observation model can be derived by differentiating the phase observation model (Equation 10) with respect to time. In practice we can employ a finite difference approximation using subsequent carrier phase observations, $\Delta\Phi^s$ (*Misra and Enge*, 2011; *Gaglione*, 2015; *Grapenthin et al.*, 2018b):

$$\Delta\Phi^s = (\mathbf{v}^s - \mathbf{v}_u) * \mathbf{1}^s + \dot{b} + \delta\epsilon_\Phi \tag{21}$$

where $(\mathbf{v}^s - \mathbf{v}_u) * \mathbf{1}^s$ is the change in range between satellite and receiver between the two observations in terms of satellite velocity, $\mathbf{v}^s$, and receiver velocity, $\mathbf{v}_u$, which the unit vector, $\mathbf{1}^s$, projects onto the satellite-receiver line of sight. The difference of satellite and receiver clock bias are captured by $\dot{b}$, and $\delta\epsilon_\Phi$ represents the differenced error terms. By using orbit information (broadcast or higher quality post-processed products), we can remove the average satellite velocity and its clock drift over the two epochs. This yields the average Doppler shift, D^s, of satellite s induced by receiver motion at velocity $\mathbf{v}_u$:

$$D^s = \text{-}\mathbf{1}^s * \mathbf{v}_u + \dot{b}_u + \delta\epsilon_\Phi \tag{22}$$

While some GNSS receivers produce this observable directly, tests show that it is not as precise as the phase differenced approach (e.g., *Gaglione*, 2015). If we have such observations from at least 4 satellites, we again can set up a linear system of equations:

$$\mathbf{D} = \mathbf{G} \begin{bmatrix} \mathbf{v}_u \\ \dot{b}_u \end{bmatrix} + \delta\epsilon_\Phi \qquad (23)$$

where $\mathbf{D}$ is a vector of Doppler shift observations and $\mathbf{G}$ is the system matrix that contains unit vectors to project the receiver velocities $\mathbf{v}_u = [v_x, v_y, v_z]^T$ onto the line of sight to the satellite. We can now estimate receiver velocity, $\mathbf{v}_u$, and receiver clock bias, $\dot{b}_u$, with standard least-squares techniques (e.g., *Aster et al.*, 2018). Note that Equation 23 has no frequency dependency; it can contain single-frequency observations or combinations of observables from different bands. The resulting velocity will be relative to an earth-centered-earth-fixed reference frame, which is straightforward to rotate into a local north-east-up reference frame (see Section 3.1 and *Bock and Melgar*, 2016).

5.2 Application

Figure 12 shows how instantaneous velocities can characterize an earthquake. Here, we again use 5 Hz GNSS observations of the 2015 M_w 7.8 Gorkha, Nepal, earthquake from *Galetzka et al.* (2015) to generate L2-only velocities from final IGS orbits (*Dow et al.*, 2009) and plot only the north component. Most striking is the difference in response at KKN4 and CHLM, the two sites closest to the epicenter (black star), compared to NAST. The latter is located in the Kathmandu Basin and shows a significantly longer response due to seismic energy trapped and reverberating within the basin.

To convince ourselves that the, in this case single-frequency, instantaneous velocities are a precise estimate of ground motion, we can compare them to the previously generated (Figure 8) post-processed kinematic positioning solutions at NAST and KKN4 (Figure 13). The east component of the instantaneous velocities is shown in black in the left panels while the red lines are the differentiated displacements from Figure 8. These two velocity records track each other very well. The main difference is some higher frequency noise in the single-frequency instantaneous velocities, which results in the drift errors common to seismic data integrated to displacements. We can see this in the right panels in Figure 13 where we have done just this and compare the integrated instantaneous velocities to GPS displacements. Fitting and removing a polynomial from the time series up to the earthquake origin time allows us to detrend and remove the drift from the integrated velocities such that these displacements track the positioning derived displacements very well. Differencing the averages over ~20 seconds of pre-event and post-event values for integrated velocities and absolute displacements yields misestimations of 8.2 cm and 14.1 cm of horizontal and -3.6 cm and -11.0 cm of vertical displacements at NAST and KKN4, respectively, which are 6-8% of the error from the total co-seismic offset. This is similar to the errors *Melgar et al.* (2019) observe when comparing real-time and post-processed kinematic positioning solutions for the 2019 Ridgecrest event. It is important to reiterate that the instantaneous velocities were derived without a very
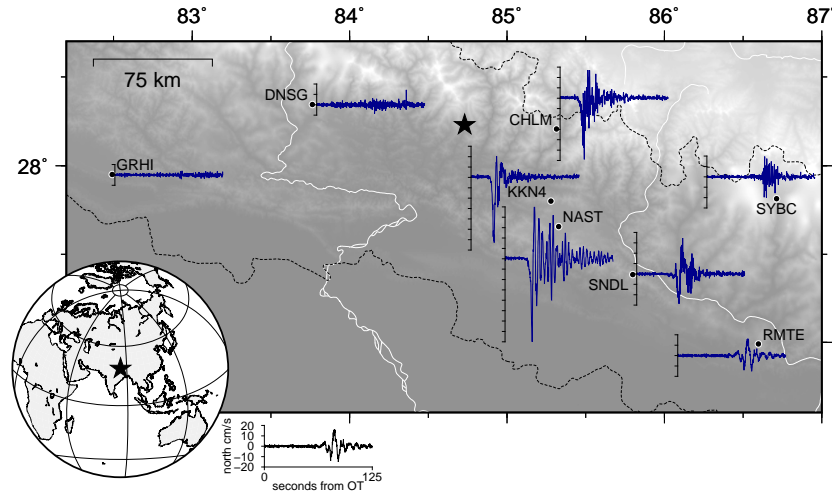
Fig. 12 North instantaneous GNSS velocities derived from 5 Hz GNSS following the M_w 7.8 Gorkha, Nepal, earthquake in 2015. Scale at the bottom is in cm/s; maximum velocities are on the order of 80 cm/s. NAST in Kathmandu Basin shows clear basin reverberation effects compared to the bedrock site KKN4.

precise a-priori position, ionosphere or troposphere corrections, ambiguity resolution, and with just single frequency data (albeit L2), while the absolute displacements are a post-processed precision product (see Section 4). This quality is achievable in real-time, simple to implement for on-receiver processing, and with potential for applications in hazard mitigation and characterization where change in position is sufficient and absolute position time series are often not necessary.

6 GNSS Reflectometry

GNSS reflectometry is a remote sensing technique, developed over the last two decades, that focuses on the analysis and interpretation of GNSS signals reflected off of the Earth's surface. Some initial applications related changes in correlation power to sea surface roughness (*Garrison et al.*, 1998), determined ocean wind speed and direction (*Armatys et al.*, 2000), or sea ice properties from the reflected signal power (*Komjathy et al.*, 2000). While some of these applications used colocated upward and downward facing GNSS antennas, more recent applications exploit direct and indirect signal interference patterns for single, upward facing antenna installations. Hence, enabling the use of these techniques at any suitable, existing GNSS site and all of its historic data. These unconventional environmental sensing techniques provide access to up to an ~1000 m^2 footprint of observations around a GNSS antenna at ~2 m height.
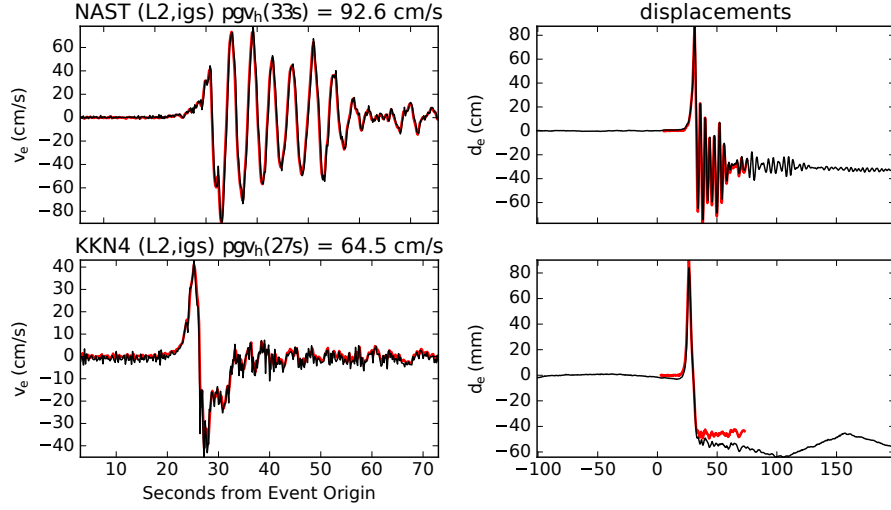
Fig. 13 Comparison of east velocities and displacements at stations NAST (top) and KKN4 (bottom) for the Gorkha earthquake (see Figure 12). **(left)** L2 instavels (black) and differentiated displacements inferred from positioning solutions (red) with excellent match. Maximum inferred horizontal peak ground velocity (pgv_h, using east and north) and their time with respect to origin is given in title bars. **(right)** L2 instavels integrated to displacements (black, fit to pre-earthquake drift removed) and positioning solutions (red). Note different time scales between columns. Instavels capture the characteristics of this earthquake very well without application of atmospheric or other models.

Instead of using the phase and range observables discussed above, *Larson et al.* (2008) suggest to use the signal-to-noise ratio (SNR, ratio of signal power to measurement noise) observable routinely recorded by GNSS receivers. However, SNR reporting across manufacturers is not standardized and measurements are sometimes discretized at 1 db-Hz intervals (*Bilich et al.*, 2007), which can render the data unsuitable for the methods described here. While the SNR measurements are not useful for positioning, they record the same interference signal between direct and indirect signal that is recorded in the other observables. *Larson and Small* (2014) have demonstrated for the entire EarthScope PBO GNSS network that interference between direct and ground-reflected satellite signals offers a means to sense the environment for changes in soil moisture (predominantly phase shift in interference pattern; *Larson et al.* (2007)), vegetation height / water content (amplitude of interference pattern smaller with higher vegetation; *Small et al.* (2010)), as well as snow depth or ocean tides (frequency change of the interference pattern, frequency increases as antenna height decreases; *Larson et al.* (2009); *Larson* (2013)). Compared to conventional positioning, SNR interference observations can be analyzed along each satellite ground track individually without requiring joint analysis of observations for multiple satellites. Thus, the footprint sensed by an individual GPS station can be visualized with antenna height and satellite-elevation dependent Fres-

nel zones (e.g., Figure 2 in *Larson*, 2016). Soil moisture estimates are an average along the satellite ground track and should be averaged over multiple satellite tracks.
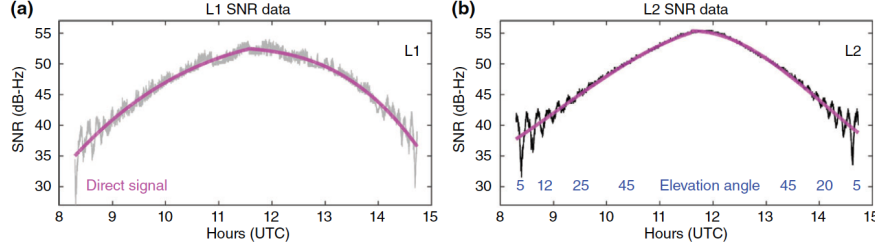
Fig. 14 SNR data for GPS L1 (a) and GPS L2 (b). The magenta polynomial fit represents the direct signal, which should be removed to utilize the SNR data for environmental sensing. The multipath signal is strongest at low elevation angles (blue axes labels). If phase, amplitude or frequency of the multipath change over time, the properties of the reflector must have changed accordingly. From: *Larson* (2016).

6.1 SNR Model

The multipath interference between planar-reflected (*Georgiadou and Kleusberg*, 1988) and direct SNR can be modeled as (*Larson*, 2016):

$$SNR = A(e)\cos(\frac{4\pi h}{\lambda}\sin(e) + \phi) \tag{24}$$

where A is the amplitude, h is the height of the antenna phase center above the ground, λ is signal wavelength (e.g., GPS L1 or L2), e is the satellite elevation angle, and ϕ is phase offset. After converting SNR observations from db-Hz to a linear scale (volts/volts), a lower order polynomial is removed to detrend the data (signal strength increases as satellites rise to nadir, Figure 14). From the remaining interference pattern phase and amplitude can be calculated through least squares estimation (e.g., *Chew et al.*, 2016). *Larson et al.* (2008) observed strong correlations between ϕ and in-situ soil moisture measurements and *Chew et al.* (2014) showed in a modeling study that phase, ϕ, is most affected by soil moisture changes. *Chew et al.* (2015) showed in a different modeling study that, while soil moisture also affects the interference signal amplitude, A, it is actually mostly affected by vegetation permittivity and height, which also affects the phase. In summary, the signal we are interested in is affected not only by soil moisture, but also surface roughness (including slope) and vegetation. *Chew et al.* (2016) present an algorithm for soil moisture retrieval from GPS SNR measurements that removes vegetation effects by estimating vegetation impact from the signal amplitude, predicting its impact on phase using the models from *Chew et al.* (2015), and removing it from the

measurements. Given the nature of the GPS signals, the soil moisture measurements are sensitive to volumetric near-surface soil moisture to a depth of at most 5 cm, important for driving evaporation.

6.2 Applications

The ability to infer changes in the reflector height from SNR changes has probably gotten the most attention. The initial application was snow depth estimation (see below), but since then additional processes changing the reflector height around the GPS antenna have been explored such has decadal changes of permafrost (*Liu and Larson*, 2018) and notably ocean tides (*Larson*, 2013; *Larson et al.*, 2017) with an extension to storm surges (*Peng et al.*, 2019). The latter simply require a GNSS monument with partial view of the ocean and SNR-based reflector height analysis only for satellite signals from this azimuth. Since every satellite can be evaluated independently, this is easily achievable. Measurements of sea level with GNSS are very attractive as these are automatically tied into a global reference frame. The positioning solutions provide any changes in land surface elevation in this reference frame, which allows to untangle sea level height changes and land changes due to, for instance, glacial isostatic adjustment or tectonics.

Larson et al. (2009) showed for a GNSS site installed at a research site in Colorado that antennas with reflection suppression, installed for tectonic studies, can be used in reflection studies to measure snow depth (Figure 15). It is clear that the frequency decreases with the addition of the observed 35 cm of new snow, as expected from $f = \frac{4\pi h}{\lambda}$ in Equation 24 (Figure 15a) in two subsequent days of observations. Modeled SNR data for the same time and snow accumulation as in the data reproduces the observations well (Figure 15b), confirming that the reflector moved 35 cm closer to the antenna.

The retrieval of ocean tidal heights from GNSS reflections shown in Figure 16 is an extension of the work on antenna heights above a reflector discussed above. *Larson* (2013) found that a GPS station, located on a small island in Katchemak Bay, Alaska, and installed to constrain tectonic motion was so close to the ocean that some satellite signals got reflected off the ocean. Since we can consider tides to move the reflector towards or away from the antenna, the SNR observations from the ocean-reflected signals can be used to solve for the tidal height. *Larson* (2013) did just that and compared the GPS-inferred tidal height to a nearby tide gauge (Figure 16) and found that the agreement between both is 2.3 cm for daily mean sea levels.

Fig. 15 (a) GPS SNR measurements (direct signal removed) on two subsequent days for satellite PRN7 before (red) and after (black) 35 cm of snow fall. (b) GPS multipath model predictions for the same times assuming 35 cm new snow with density 240 kg m^{-3}. From: *Larson et al.* (2009).
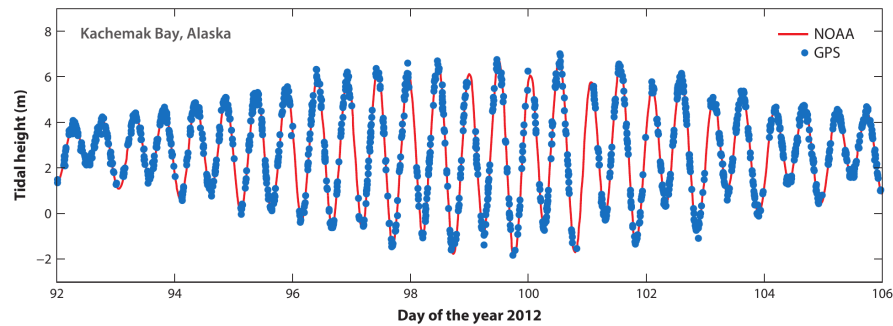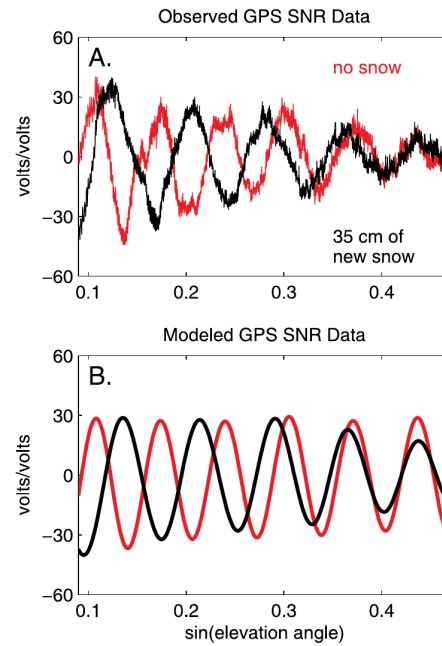
Fig. 16 Tidal heights at Katchemak Bay, Alaska, measuren with GPS-SNR (blue) and compared to a nearby National Oceanic and Atmospheric Administration (NOAA) tide gauge (red) at Seldovia, Alaska, about 30 km away. From: *Larson* (2019).

7 Parting Thoughts

GNSS is a powerful and exceptionally versatile tool, which, due to its widespread global use, is unlikely to disappear. Its contributions to civil life range from precision agriculture, global time synchronization and aviation to finding a restaurant. These society-permeating applications add to the strong defense interests in maintaining satellite navigation systems. In the geosciences, satellite navigation system applications go far beyond timing and positioning. Analyses of the ionosphere, troposphere,

and local environmental sensing have been proven robust. Modernized signals at higher signal strength will likely open further applications.

8 Acknowledgements

References

Agnew, D. C., and K. M. Larson, Finding the repeat times of the GPS constellation, *GPS Solutions*, *11*(1), 71–76, doi:10.1007/s10291-006-0038-4, 2006.

Altamimi, Z., P. Rebischung, L. Métivier, and X. Collilieux, ITRF2014: A new release of the International Terrestrial Reference Frame modeling nonlinear station motions, *Journal of Geophysical Research: Solid Earth*, *121*(8), 6109–6131, doi: 10.1002/2016JB013098, 2016.

Amos, C. B., P. Audet, W. C. Hammond, R. Bürgmann, I. a. Johanson, and G. Blewitt, Uplift and seismicity driven by groundwater depletion in central California., *Nature*, *509*(7501), 483–486, doi:10.1038/nature13275, 2014.

Anderson, K. R., I. A. Johanson, M. R. Patrick, M. Gu, P. Segall, M. P. Poland, E. K. Montgomery-Brown, and A. Miklius, Magma reservoir failure and the onset of caldera collapse at Kīlauea Volcano in 2018, *Science*, *366*(6470), eaaz1822, doi:10.1126/science.aaz1822, 2019.

Apel, E. V., R. Bürgmann, G. M. Steblov, N. Vasilenko, R. King, and A. Prytkov, Independent active microplate tectonics of northeast Asia from GPS velocities and block modeling, *Geophys. Res. Lett.*, *33*, L11,303, doi:10.1029/2006GL026077, 2006.

Argus, D. F., and M. B. Heflin, Plate motion and crustal deformation estimated with geodetic data from the Global Positioning System, *Geophysical Research Letters*, *22*(15), 1973–1976, doi:10.1029/95GL02006, 1995.

Argus, D. F., R. G. Gordon, M. B. Heflin, C. Ma, R. J. Eanes, P. Willis, W. R. Peltier, and S. E. Owen, The angular velocities of the plates and the velocity of Earth's centre from space geodesy, *Geophysical Journal International*, *180*, 913–960, doi:10.1111/j.1365-246X.2009.04463.x, 2010.

Argus, D. F., Y. Fu, and F. W. Landerer, Seasonal variation in total water storage in California inferred from GPS observations of vertical land motion, *Geophys. Res. Lett.*, *41*, 1971–1980, doi:10.1002/2014GL059570, 2014.

Armatys, M., A. Komjathy, P. Axelrad, and S. J. Katzberg, A comparison of GPS and scatterometer sensing of ocean wind speed and direction, in *IGARSS 2000. IEEE 2000 International Geoscience and Remote Sensing Symposium. Taking the Pulse of the Planet: The Role of Remote Sensing in Managing the Environment. Proceedings (Cat. No. 00CH37120)*, vol. 7, pp. 2861–2863, IEEE, doi:10.1017/CBO9781107415324.004, 2000.

Artru, J., V. Ducic, H. Kanamori, P. Lognonné, and M. Murakami, Ionospheric detection of gravity waves induced by tsunamis, *Geophysical Journal International*, *160*(3), 840–848, doi:10.1111/j.1365-246X.2005.02552.x, 2005.

Aster, R. C., B. Borchers, and C. H. Thurber, *Parameter Estimation and Inverse Problems*, 3rd ed. ed., 404 pp., Elsevier, 2018.

Axelrad, P., C. Comp, and P. Macdoran, SNR-based multipath error correction for GPS differential phase, *IEEE Transactions on Aerospace and Electronic Systems*, *32*(2), 650–660, doi:10.1109/7.489508, 1996.

Bevis, M., S. Businger, T. A. Herring, C. Rocken, R. A. Anthes, and R. H. Ware, GPS Meteorology: Remote Sensing of Atmospheric Water Vapor Using the Global Positioning System, *Journal of Geophysical Research*, *97*(D14), 15,715–787,801, 1992.

Bilham, R., V. K. Gaur, and P. Molnar, Himalayan Seismic Hazard, *Science*, *293*, 1442–1444, 2001.

Bilich, A., P. Axelrad, and K. M. Larson, Scientific utility of the signal-to-noise ratio (SNR) reported by geodetic GPS receivers, *20th International Technical Meeting of the Satellite Division of The Institute of Navigation 2007 ION GNSS 2007*, *2*, 1999–2010, 2007.

Blewitt, G., Carrier phase ambiguity resolution for the Global Positioning System applied to geodetic baselines up to 2000 km, *Journal of Geophysical Research: Solid Earth*, *94*(B8), 10,187–10,203, doi:10.1029/JB094iB08p10187, 1989.

Blewitt, G., D. Lavallée, P. Clarke, and K. Nurutdinov, A New Global Mode of Earth Deformation: Seasonal Cycle Detected, *Science*, *294*, 2342–2345, 2001.

Blewitt, G., C. Kreemer, W. C. Hammond, and J. M. Goldfarb, Terrestrial reference frame NA12 for crustal deformation studies in North America, *Journal of Geodynamics*, *72*, 11–24, doi:10.1016/j.jog.2013.08.004, 2013.

Bock, Y., and D. Melgar, Physical applications of GPS geodesy: a review, *Reports on Progress in Physics*, *79*(10), 106,801, doi:10.1088/0034-4885/79/10/106801, 2016.

Bock, Y., D. Melgar, and B. W. Crowell, Real-Time Strong-Motion Broadband Displacements from Collocated GPS and Accelerometers, *Bulletin of the Seismological Society of America*, *101*(6), 2904–2925, doi:10.1785/0120110007, 2011.

Boehm, J., A. Niell, P. Tregoning, and H. Schuh, Global Mapping Function (GMF): A new empirical mapping function based on numerical weather model data, *Geophys. Res. Lett.*, *33*, L07,304, doi:10.1029/2005GL025546, 2006a.

Boehm, J., B. Werl, and H. Schuh, Troposphere mapping functions for GPS and very long baseline interferometry from European Centre for Medium-Range Weather Forecasts operational analysis data, *Journal of Geophysical Research: Solid Earth*, *111*(2), 1–9, doi:10.1029/2005JB003629, 2006b.

Boehm, J., R. Heinkelmann, and H. Schuh, Short Note: A global model of pressure and temperature for geodetic applications, *J. Geod.*, *81*, 679–683, doi: 10.1007/s00190-007-0135-3, 2007.

Borsa, A. A., D. C. Agnew, and D. R. Cayan, Ongoing drought-induced uplift in the western United States, *Science*, *345*(6204), 1587–1590, doi: 10.1126/science.1260279, 2014.

Calais, E., and J. B. Minster, GPS detection of ionospheric perturbations following the January 17, 1994, Northridge Earthquake, *Geophysical Research Letters*, *22*(9), 1045–1048, doi:10.1029/95GL00168, 1995.

Cervelli, B. P. F., T. J. Fournier, J. T. Freymueller, J. A. Power, M. Lisowski, and B. A. Pauk, Geodetic Constraints on Magma Movement and Withdrawal During the 2006 Eruption of Augustine Volcano, in *The 2006 Eruption of Augustine Volcano, Alaska, USGS Professional Paper 1769*, edited by J. A. Power, M. L. Coombs, and J. T. Freymueller, chap. 17, pp. 427–452, USGS, 2006.

Chew, C., E. E. Small, and K. M. Larson, An algorithm for soil moisture estimation using GPS-interferometric reflectometry for bare and vegetated soil, *GPS Solutions*, *20*(3), 525–537, doi:10.1007/s10291-015-0462-4, 2016.

Chew, C. C., E. E. Small, K. M. Larson, and V. U. Zavorotny, Effects of Near-Surface Soil Moisture on GPS SNR Data: Development of a Retrieval Algorithm for Soil Moisture, *IEEE Transactions on Geoscience and Remote Sensing*, *52*(1), 537–543, doi:10.1109/TGRS.2013.2242332, 2014.

Chew, C. C., E. E. Small, K. M. Larson, and V. U. Zavorotny, Vegetation Sensing Using GPS-Interferometric Reflectometry: Theoretical Effects of Canopy Parameters on Signal-to-Noise Ratio Data, *IEEE Transactions on Geoscience and Remote Sensing*, *53*(5), 2755–2764, doi:10.1109/TGRS.2014.2364513, 2015.

Choi, K., A. Bilich, K. M. Larson, and P. Axelrad, Modified sidereal filtering: Implications for high-rate GPS positioning, *Geophysical Research Letters*, *31*(22), L22,608, doi:10.1029/2004GL021621, 2004.

Colosimo, G., M. Crespi, and A. Mazzoni, Real-time GPS seismology with a stand-alone receiver: A preliminary feasibility demonstration, *Journal of Geophysical Research: Solid Earth*, *116*(B11), n/a–n/a, doi:10.1029/2010JB007941, 2011.

Copley, A., J. P. Avouac, and B. P. Wernicke, Evidence for mechanical coupling and strong Indian lower crust beneath southern Tibet, *Nature*, *472*(7341), 79–81, doi:10.1038/nature09926, 2011.

Counselman, C. C., and S. A. Gourevitch, Miniature Interferometer Terminals for Earth Surveying: Ambiguity and Multipath with Global Positioning System, *IEEE Transactions on Geoscience and Remote Sensing*, *GE-19*(4), 244–252, doi: 10.1109/TGRS.1981.350379, 1981.

Counselman, C. C., I. I. Shapiro, R. L. Greenspan, and D. B. J. Cox, Backpack VLBI Terminal with Subcentimeter Capabilityh, in *Proc. RadioInterferometric Tech-*

niques for Geodesy, vol. vol. 2115, pp. 409–413, NASA Conference Publication, 1980.

Decker, L., World Geodetic System 1984, in *Proceedings of the Fourth International Geodetic Symposium on Satellite Positioning*, vol. 1, pp. 69–92, St Louis, MO, 1986.

Desai, S. D., and A. E. Sibois, Evaluating predicted diurnal and semidiurnal tidal variations in polar motion with GPS-based observations, *Journal of Geophysical Research: Solid Earth*, *121*(7), 5237–5256, doi:10.1002/2016JB013125, 2016.

Dixon, T. H., A. Mao, M. Bursik, M. Heflin, J. Langbein, R. Stein, and F. Webb, Continuous monitoring of surface deformation at Long Valley Caldera, California, with GPS, *Journal of Geophysical Research: Solid Earth*, *102*(B6), 12,017–12,034, doi:10.1029/96JB03902, 1997.

Dong, D.-N., and Y. Bock, Global Positioning System Network analysis with phase ambiguity resolution applied to crustal deformation studies in California, *Journal of Geophysical Research: Solid Earth*, *94*(B4), 3949–3966, doi:10.1029/JB094iB04p03949, 1989.

Dow, J. M., R. E. Neilan, and C. Rizos, The International GNSS Service in a changing landscape of Global Navigation Satellite Systems, *J. Geod.*, *83*, 191–198, doi:10.1007/s00190-008-0300-3, 2009.

Dragert, G., K. Wang, and T. S. James, A silent slip event on the deeper Cascadia subduction interface., *Science (New York, N.Y.)*, *292*(5521), 1525–1528, doi:10.1126/science.1060152, 2001.

Easton, R. L., Navigation system using satellites and passive ranging techniques, 1974.

Elliott, J. L., C. F. Larsen, J. T. Freymueller, and R. J. Motyka, Tectonic block motion and glacial isostatic adjustment in southeast Alaska and adjacent Canada constrained by GPS measurements, *Journal of Geophysical Research*, *115*(B9), B09,407, doi:10.1029/2009JB007139, 2010.

Elsworth, D., G. Mattioli, J. Taron, B. Voight, and R. Herd, Implications of magma transfer between multiple reservoirs on eruption cycling., *Science (New York, N.Y.)*, *322*(5899), 246–248, doi:10.1126/science.1161297, 2008.

Feigl, K. L., D. C. Agnew, Y. Bock, D. Dong, A. Donnellan, B. H. Hager, T. A. Herring, D. D. Jackson, T. H. Jordan, R. W. King, S. Larsen, K. M. Larson, M. H. Murray, Z. Shen, and F. H. Webb, Space geodetic measurement of crustal deformation in central and southern California, 1984-1992, *Journal of Geophysical Research: Solid Earth*, *98*(B12), 21,677–21,712, doi:10.1029/93JB02405, 1993.

Fitzgerald, T., Observations of total electron content perturbations on GPS signals caused by a ground level explosion, *Journal of Atmospheric and Solar-Terrestrial Physics*, *59*(7), 829–834, doi:10.1016/S1364-6826(96)00105-8, 1997.

Fletcher, H. J., and J. T. Freymueller, New GPS constraints on the motion of the Yakutat Block, *Geophysical Research Letters*, *26*(19), 3029–3032, doi:10.1029/1999GL005346, 1999.

Fournier, T., J. Freymueller, and P. Cervelli, Tracking magma volume recovery at Okmok volcano using GPS and an unscented Kalman filter, *Journal of Geophysical Research*, *114*(B2), B02,405, doi:10.1029/2008JB005837, 2009.

Freymueller, J. T., H. Woodard, S. C. Cohen, R. Cross, J. Elliott, C. F. Larsen, S. Hreinsdóttir, and C. Zweck, Active Deformation Processes in Alaska, Based on 15 Years of GPS Measurements, in *Active Tectonics and Seismic Potential of Alaska*, edited by J. T. Freymueller, P. J. Haeussler, R. L. Wesson, and G. Ekström, Geophysical Monograph, pp. 1–42, AGU, 2008.

Fu, Y., and J. T. Freymueller, Seasonal and long-term vertical deformation in the Nepal Himalaya constrained by GPS and GRACE measurements, *Journal of Geophysical Research: Solid Earth*, *117*(B3), B03,407, doi:10.1029/2011JB008925, 2012.

Fu, Y., J. T. Freymueller, and T. van Dam, The effect of using inconsistent ocean tidal loading models on GPS coordinate solutions, *Journal of Geodesy*, *86*(6), 409–421, doi:10.1007/s00190-011-0528-1, 2012.

Fu, Y., D. F. Argus, and F. W. Landerer, GPS as an independent measurement to estimate terrestrial water storage variations in Washington and Oregon, *Journal of Geophysical Research: Solid Earth*, *120*(1), 552–566, doi: 10.1002/2014JB011415, 2015.

Gaglione, S., How does a GNSS receiver estimate velocity?, *Inside GNSS*, pp. 38–41, 2015.

Galetzka, J., D. Melgar, J. F. Genrich, J. Geng, S. Owen, E. O. Lindsey, X. Xu, Y. Bock, J. P. Avouac, L. B. Adhikari, B. N. Upreti, B. Pratt-Sitaula, T. N. Bhattarai, B. P. Sitaula, A. Moore, K. W. Hudnut, W. Szeliga, J. Normandeau, M. Fend, M. Flouzat, L. Bollinger, P. Shrestha, B. Koirala, U. Gautam, M. Bhatterai, R. Gupta, T. Kandel, C. Timsina, S. N. Sapkota, S. Rajaure, and N. Maharjan, Slip pulse and resonance of the Kathmandu basin during the 2015 Gorkha earthquake, Nepal, *Science*, doi:10.1126/science.aac6383, 2015.

Garrison, J. L., S. J. Katzberg, and M. I. Hill, Effect of sea roughness on bistatically scattered range coded signals from the Global Positioning System, *Geophysical Research Letters*, *25*(13), 2257–2260, doi:10.1029/98GL51615, 1998.

Geng, J., Y. Bock, D. Melgar, B. W. Crowell, and J. S. Haase, A new seismogeodetic approach applied to GPS and accelerometer observations of the 2012 Brawley seismic swarm: Implications for earthquake early warning, *Geochemistry, Geophysics, Geosystems*, *14*(7), 2124–2142, doi:10.1002/ggge.20144, 2013.

Geng, J., Y. Pan, X. Li, J. Guo, J. Liu, X. Chen, and Y. Zhang, Noise Characteristics of High-Rate Multi-GNSS for Subdaily Crustal Deformation Monitoring, *Journal of Geophysical Research: Solid Earth*, *123*(2), 1987–2002, doi: 10.1002/2018JB015527, 2018.

Geng, J., J. Guo, H. Chang, and X. Li, Toward global instantaneous decimeter-level positioning using tightly coupled multi-constellation and multi-frequency GNSS, *Journal of Geodesy*, *93*(7), 977–991, doi:10.1007/s00190-018-1219-y, 2019.

Georgiadou, Y., and A. Kleusberg, On carrier signal multipath effects in relative GPS positioning, *Manuscripta geodaetica*, *13*(3), 172–179, 1988.

Gérard, P., and B. Luzum, IERS Conventions (2010), *Tech. rep.*, International Earth Rotation and Reference Systems Service, 2011.

Grapenthin, R., and J. T. Freymueller, The dynamics of a seismic wave field: Animation and analysis of kinematic GPS data recorded during the 2011

Tohoku-oki earthquake, Japan, *Geophysical Research Letters*, *38*(18), 1–5, doi: 10.1029/2011GL048405, 2011.

Grapenthin, R., F. Sigmundsson, H. Geirsson, T. Árnadóttir, and V. Pinel, Icelandic rhythmics: Annual modulation of land elevation and plate spreading by snow load, *Geophysical Research Letters*, *33*(24), doi:10.1029/2006GL028081, 2006.

Grapenthin, R., J. T. Freymueller, and A. M. Kaufman, Geodetic observations during the 2009 eruption of Redoubt Volcano, Alaska, *Journal of Volcanology and Geothermal Research*, *259*, 115–132, doi:10.1016/j.jvolgeores.2012.04.021, 2013.

Grapenthin, R., I. Johanson, and R. M. Allen, The 2014 Mw 6.0 Napa earthquake, California: Observations from real-time GPS-enhanced earthquake early warning, *Geophysical Research Letters*, *41*(23), 8269–8276, doi:10.1002/2014GL061923, 2014a.

Grapenthin, R., I. A. Johanson, and R. M. Allen, Operational real-time GPS-enhanced earthquake early warning, *Journal of Geophysical Research: Solid Earth*, *119*(10), 7944–7965, doi:10.1002/2014JB011400, 2014b.

Grapenthin, R., S. Hreinsdóttir, and A. Van Eaton, Volcanic Hail Detected With GPS: The 2011 Eruption of Grímsvötn Volcano, Iceland, *Geophysical Research Letters*, *45*(22), doi:10.1029/2018GL080317, 2018a.

Grapenthin, R., M. West, M. Gardine, C. Tape, and J. Freymueller, Single-frequency instantaneous GNSS velocities resolve dynamic ground motion of the 2016 M$_w$ 7.1 Iniskin, Alaska, Earthquake, *Seismological Research Letters*, *89*(3), doi:10.1785/0220170235, 2018b.

Gudmundsson, M. T., K. Jónsdóttir, A. Hooper, E. P. Holohan, S. A. Halldórsson, B. G. Ófeigsson, S. Cesca, K. S. Vogfjörd, F. Sigmundsson, T. Högnadóttir, P. Einarsson, O. Sigmarsson, A. H. Jarosch, K. Jónasson, E. Magnússon, S. Hreinsdóttir, M. Bagnardi, M. M. Parks, V. Hjörleifsdóttir, F. Pálsson, T. R. Walter, M. P. J. Schöpfer, S. Heimann, H. I. Reynolds, S. Dumont, E. Bali, G. H. Gudfinnsson, T. Dahm, M. J. Roberts, M. Hensch, J. M. C. Belart, K. Spaans, S. Jakobsson, G. B. Gudmundsson, H. M. Fridriksdóttir, V. Drouin, T. Dürig, G. Aðalgeirsdóttir, M. S. Riishuus, G. B. M. Pedersen, T. van Boeckel, B. Oddsson, M. A. Pfeffer, S. Barsotti, B. Bergsson, A. Donovan, M. R. Burton, and A. Aiuppa, Gradual caldera collapse at Bárdarbunga volcano, Iceland, regulated by lateral magma outflow, *Science*, *353*(6296), aaf8988, doi:10.1126/science.aaf8988, 2016.

Hadas, T., and J. Bosy, IGS RTS precise orbits and clocks verification and quality degradation over time, *GPS Solutions*, *19*(1), 93–105, doi:10.1007/s10291-014-0369-5, 2015.

Heki, K., Seasonal Modulation of Interseismic Strain Buildup in Northeastern Japan Driven by Snow Loads, *Science*, *293*(5527), 89–92, doi:10.1126/science.1061056, 2001.

Heki, K., Explosion energy of the 2004 eruption of the Asama Volcano, central Japan, inferred from ionospheric disturbances, *Geophysical Research Letters*, *33*(14), 2–5, doi:10.1029/2006GL026249, 2006.

Herring, T. A., D. Dong, and R. W. King, Sub-milliarcsecond determination of pole position using Global Positioning System data, *Geophysical Research Letters*, *18*(10), 1893–1896, doi:10.1029/91GL02306, 1991.

Herring, T. A., R. W. King, and S. C. McClusky, GAMIT/GLOBK Reference Manuals, Release 10.4, 2010.

Herring, T. A., T. I. Melbourne, M. H. Murray, M. A. Floyd, W. M. Szeliga, R. W. King, D. A. Phillips, C. M. Puskas, M. Santillan, and L. Wang, Plate Boundary Observatory and related networks: GPS data analysis methods and geodetic products, *Reviews of Geophysics*, *54*(4), 759–808, doi:10.1002/2016RG000529, 2016.

Hoffmann-Wellenhof, B., H. Lichtenegger, and E. Wasle, *GNSS - Global Navigation Satellite Systems*, 546 pp., Springer Vienna, Vienna, doi:10.1007/978-3-211-73017-1, 2008.

Houlié, N., P. Briole, A. Nercessian, and M. Murakami, Sounding the plume of the 18 August 2000 eruption of Miyakejima volcano (Japan) using GPS, *Geophysical Research Letters*, *32*(5), L05,302, doi:10.1029/2004GL021728, 2005.

Hreinsdóttir, S., F. Sigmundsson, M. J. Roberts, H. Björnsson, R. Grapenthin, P. Arason, T. Árnadóttir, J. Hólmjárn, H. Geirsson, R. A. Bennett, M. T. Gudmundsson, B. Oddsson, B. G. Ófeigsson, T. Villemin, T. Jónsson, E. Sturkell, Á. Höskuldsson, G. Larsen, T. Thordarson, and B. A. Óladóttir, Volcanic plume height correlated with magma-pressure change at Grímsvötn Volcano, Iceland, *Nature Geoscience*, *7*(3), 214–218, doi:10.1038/ngeo2044, 2014.

Hunter, J. D., Matplotlib: A 2D graphics environment, *Computing in Science and Engineering*, *9*(3), 99–104, doi:10.1109/MCSE.2007.55, 2007.

Jansma, P. E., G. S. Mattioli, A. Lopez, C. DeMets, T. H. Dixon, P. Mann, and E. Calais, Neotectonics of Puerto Rico and the Virgin Islands, northeastern Caribbean, from GPS geodesy, *Tectonics*, *19*(6), 1021–1037, doi:10.1029/1999TC001170, 2000.

Komjathy, A., J. Maslanik, V. Zavorotny, P. Axelrad, and S. Katzberg, Sea ice remote sensing using surface reflected GPS signals, in *IGARSS 2000. IEEE 2000 International Geoscience and Remote Sensing Symposium. Taking the Pulse of the Planet: The Role of Remote Sensing in Managing the Environment. Proceedings (Cat. No.00CH37120)*, vol. 7, pp. 2855–2857, IEEE, doi:10.1109/IGARSS.2000.860270, 2000.

Kreemer, C., G. Blewitt, and E. C. Klein, A geodetic plate motion and Global Strain Rate Model, *Geochemistry, Geophysics, Geosystems*, *15*(10), 3849–3889, doi:10.1002/2014GC005407, 2014.

Lagler, K., M. Schindelegger, J. Böhm, H. Krásná, and T. Nilsson, GPT2: Empirical slant delay model for radio space geodetic techniques, *Geophysical Research Letters*, *40*(6), 1069–1073, doi:10.1002/grl.50288, 2013.

Larson, K. M., A new way to detect volcanic plumes, *Geophysical Research Letters*, *40*(11), 2657–2660, doi:10.1002/grl.50556, 2013.

Larson, K. M., GPS interferometric reflectometry: applications to surface soil moisture, snow depth, and vegetation water content in the western United States, *Wiley Interdisciplinary Reviews: Water*, *3*(6), 775–787, doi:10.1002/wat2.1167, 2016.

Larson, K. M., Unanticipated Uses of the Global Positioning System, *Annual Review of Earth and Planetary Sciences*, *47*(1), 19–40, doi:10.1146/annurev-earth-053018-060203, 2019.

Larson, K. M., and E. E. Small, GPS ground networks for water cycle sensing, *2014 IEEE Geoscience and Remote Sensing Symposium*, pp. 3822–3825, doi: 10.1109/IGARSS.2014.6947317, 2014.

Larson, K. M., P. Bodin, and J. Gomberg, Using 1-Hz GPS Data to Measure Deformations Caused by the Denali Fault Earthquake, *Science*, *300*(5624), 1421–1424, doi:10.1126/science.1084531, 2003.

Larson, K. M., A. Bilich, and P. Axelrad, Improving the precision of high-rate GPS, *Journal of Geophysical Research*, *112*(B5), B05,422, doi: 10.1029/2006JB004367, 2007.

Larson, K. M., E. E. Small, E. Gutmann, A. Bilich, P. Axelrad, and J. Braun, Using GPS multipath to measure soil moisture fluctuations: initial results, *GPS Solutions*, *12*(3), 173–177, doi:10.1007/s10291-007-0076-6, 2008.

Larson, K. M., E. D. Gutmann, V. U. Zavorotny, J. J. Braun, M. W. Williams, and F. G. Nievinski, Can we measure snow depth with GPS receivers?, *Geophysical Research Letters*, *36*(17), L17,502, doi:10.1029/2009GL039430, 2009.

Larson, K. M., R. D. Ray, F. G. Nievinski, and J. T. Freymueller, The Accidental Tide Gauge: A GPS Reflection Case Study From Kachemak Bay, Alaska, *IEEE Geoscience and Remote Sensing Letters*, *10*(5), 1200–1204, doi: 10.1109/LGRS.2012.2236075, 2013.

Larson, K. M., S. Palo, C. Roesler, M. Mattia, V. Bruno, M. Coltelli, and D. Fee, Detection of plumes at Redoubt and Etna volcanoes using the GPS SNR method, *Journal of Volcanology and Geothermal Research*, *344*, 26–39, doi: 10.1016/j.jvolgeores.2017.04.005, 2017.

Lichten, S. M., Estimation and Filtering Techniques for High-Accuracy GPS Applications to monitor level motions active Initialresults experiments suggest maybeobtained equaling those from more, *The Telecommunications and Data Acquisition Report*, pp. 1–20, 1989.

Liu, L., and K. M. Larson, Decadal changes of surface elevation over permafrost area estimated using reflected GPS signals, *The Cryosphere*, *12*(2), 477–489, doi:10.5194/tc-12-477-2018, 2018.

Liu, T., Y. Yuan, B. Zhang, N. Wang, B. Tan, and Y. Chen, Multi-GNSS precise point positioning (MGPPP) using raw observations, *Journal of Geodesy*, *91*(3), 253–268, doi:10.1007/s00190-016-0960-3, 2017.

Lyard, F., F. Lefevre, T. Letellier, and O. Francis, Modelling the global ocean tides: modern insights from FES2004, *Ocean Dynamics*, *56*(5-6), 394–415, doi: 10.1007/s10236-006-0086-x, 2006.

Mannucci, A. J., B. D. Wilson, D. N. Yuan, C. H. Ho, U. J. Lindqwister, and T. F. Runge, A global mapping technique for GPS-derived ionospheric total electron content measurements, *Radio Science*, *33*(3), 565–582, doi:10.1029/97RS02707, 1998.

Melbourne, T. I., D. Melgar, B. W. Crowell, and W. M. Szeliga, Seismic Sensors in Orbit, *EOS*, *90*, 1–11, doi:10.1029/2019EO138001, 2019.

Melgar, D., T. I. Melbourne, B. W. Crowell, J. Geng, W. Szeliga, C. Scrivner, M. Santillan, and D. E. Goldberg, Real-Time High-Rate GNSS Displacements: Performance Demonstration during the 2019 Ridgecrest, California, Earthquakes, *Seismological Research Letters*, pp. 1–13, doi:10.1785/0220190223, 2019.

Meng, X., P. Vergados, A. Komjathy, and O. Verkhoglyadova, Upper Atmospheric Responses to Surface Disturbances: An Observational Perspective, *Radio Science*, *54*(11), 1076–1098, doi:10.1029/2019RS006858, 2019.

Misra, P., and P. Enge, *Global Positioning System: Signals, Measurements, and Performance - Revised Second Edition (2011)*, revised 2n ed., Ganga-Jamuna Press, Lincoln, 2011.

Montenbruck, O., O. Montenbruck, P. Steigenberger, R. Khachikyan, G. Weber, R. B. Langley, L. Mervart, and U. Hugentobler, IGS-MGEX Preparing the Ground for Multi-COnstellation GNSS Science, *Inside GNSS*, *9(1)*(January/February), 42–49, 2014.

Murray, J. R., B. W. Crowell, R. Grapenthin, K. Hodgkinson, J. O. Langbein, T. Melbourne, D. Melgar, S. E. Minson, and D. A. Schmidt, Development of a Geodetic Component for the U.S. West Coast Earthquake Early Warning System, *Seismological Research Letters*, *89*(6), 2322–2336, doi:10.1785/0220180162, 2018.

Neal, C. A., S. R. Brantley, L. Antolik, J. L. Babb, M. Burgess, K. Calles, M. Cappos, J. C. Chang, S. Conway, L. Desmither, P. Dotray, T. Elias, P. Fukunaga, S. Fuke, I. A. Johanson, K. Kamibayashi, J. Kauahikaua, R. L. Lee, S. Pekalib, A. Miklius, W. Million, C. J. Moniz, P. A. Nadeau, P. Okubo, C. Parcheta, M. R. Patrick, B. Shiro, D. A. Swanson, W. Tollett, F. Trusdell, E. F. Younger, M. H. Zoeller, E. K. Montgomery-Brown, K. R. Anderson, M. P. Poland, J. L. Ball, J. Bard, M. Coombs, H. R. Dietterich, C. Kern, W. A. Thelen, P. F. Cervelli, T. Orr, B. F. Houghton, C. Gansecki, R. Hazlett, P. Lundgren, A. K. Diefenbach, A. H. Lerner, G. Waite, P. Kelly, L. Clor, C. Werner, K. Mulliken, G. Fisher, and D. Damby, The 2018 rift eruption and summit collapse of Kīlauea Volcano, *Science*, *363*(6425), 367–374, doi:10.1126/science.aav7046, 2019.

Newman, A., Slow Deformation and Lower Seismic Hazard at the New Madrid Seismic Zone, *Science*, *284*(5414), 619–621, doi:10.1126/science.284.5414.619, 1999.

Nikolaidis, R. M., Y. Bock, P. J. de Jonge, P. Shearer, D. C. Agnew, and M. Van Domselaar, Seismic wave observations with the Global Positioning System, *J. Geophys. Res.*, *106*(B10), 21,821–897,916, 2001.

Pavlis, N. K., S. A. Holmes, S. C. Kenyon, and J. K. Factor, The development and evaluation of the Earth Gravitational Model 2008 (EGM2008), *Journal of Geophysical Research: Solid Earth*, *117*(B4), B04,406, doi:10.1029/2011JB008916, 2012.

Peng, D., E. M. Hill, L. Li, A. D. Switzer, and K. M. Larson, Application of GNSS interferometric reflectometry for detecting storm surges, *GPS Solutions*, *23*(2), 47, doi:10.1007/s10291-019-0838-y, 2019.

Rogers, G., and H. Dragert, Episodic tremor and slip on the Cascadia subduction zone: the chatter of silent slip., *Science (New York, N.Y.)*, *300*(5627), 1942–1943, doi:10.1126/science.1084783, 2003.

Segall, P., and J. L. Davis, GPS APPLICATIONS FOR GEODYNAMICS AND EARTHQUAKE STUDIES, *Annual Review of Earth and Planetary Sciences*, *25*(1), 301–336, doi:10.1146/annurev.earth.25.1.301, 1997.

Segall, P., K. R. Anderson, I. Johanson, and A. Miklius, Mechanics of Inflationary Deformation During Caldera Collapse: Evidence From the 2018 Kīlauea Eruption, *Geophysical Research Letters*, pp. 782–789, doi:10.1029/2019GL084689, 2019.

Sigmundsson, F., A. Hooper, S. Hreinsdóttir, K. S. Vogfjörd, B. G. Ófeigsson, E. R. Heimisson, S. Dumont, M. Parks, K. Spaans, G. B. Gudmundsson, V. Drouin, T. Árnadóttir, K. Jónsdóttir, M. T. Gudmundsson, T. Högnadóttir, H. M. Fridriksdóttir, M. Hensch, P. Einarsson, E. Magnússon, S. Samsonov, B. Brandsdóttir, R. S. White, T. Ágústsdóttir, T. Greenfield, R. G. Green, Á. R. Hjartardóttir, R. Pedersen, R. a. Bennett, H. Geirsson, P. C. La Femina, H. Björnsson, F. Pálsson, E. Sturkell, C. J. Bean, M. Möllhoff, A. K. Braiden, and E. P. S. Eibl, Segmented lateral dyke growth in a rifting event at Bárðarbunga volcanic system, Iceland, *Nature*, *517*(7533), 191–195, doi:10.1038/nature14111, 2015.

Silver, P. G., Y. Bock, D. C. Agnew, T. Henyey, A. T. Linde, and T. V. Mcevilly, A Plate Boundary Observatory, *IRIS Newsletter*, *XVI*(3), 1998.

Simons, M., S. E. Minson, A. Sladen, F. Ortega, J. Jiang, S. E. Owen, L. Meng, P. Ampuero, S. Wei, R. Chu, D. V. Helmberger, H. Kanamori, E. Hetland, A. W. Moore, and F. H. Webb, The 2011 Magnitude 9.0 Tohoku-Oki Earthquake: Mosaicking the Megathrust from Seconds to Centuries, *Science*, *332*, 1421–1425, doi:10.1126/science.1206731, 2011.

Small, E. E., K. M. Larson, and J. J. Braun, Sensing vegetation growth with reflected GPS signals, *Geophysical Research Letters*, *37*(12), n/a—-n/a, doi:10.1029/2010GL042951, 2010.

Teunissen, P. J., The least-squares ambiguity decorrelation adjustment: a method for fast GPS integer ambiguity estimation, *Journal of Geodesy*, doi:10.1007/BF00863419, 1995.

Teunissen, P. J. G., Least-squares estimation of the integer GPS ambiguities., 1993.

UNAVCO Community, SCIGN-PBO Nucleus GPS Network - CCCC-Cerro Coso Community College P.S., UNAVCO, GPS/GNSS Observations Dataset, doi:10.7283/Y06K-0531, 2005a.

UNAVCO Community, PBO GPS Network P595-SearlesValCS2005 P.S., UNAVCO, Inc., GPS/GNSS Observations Dataset,, doi:10.7283/T5C24TDR, 2005b.

Wallace, L. M., C. Stevens, E. Silver, R. McCaffrey, W. Loratung, S. Hasiata, R. Stanaway, R. Curley, R. Rosa, and J. Taugaloidi, GPS and seismological constraints on active tectonics and arc-continent collision in Papua New Guinea: Implications for mechanics of microplate rotations in a plate boundary zone, *Journal of Geophysical Research: Solid Earth*, *109*(B5), 1–16, doi:10.1029/2003JB002481, 2004.

Wang, Q., Present-Day Crustal Deformation in China Constrained by Global Positioning System Measurements, *Science*, *294*(5542), 574–577, doi:10.1126/science.1063647, 2001.

Wessel, P., W. H. Smith, R. Scharroo, J. Luis, and F. Wobbe, Generic mapping tools: Improved version released, *Eos*, *94*(45), 409–410, doi:10.1002/2013EO450001, 2013.

Zheng, K., X. Zhang, P. Li, X. Li, M. Ge, F. Guo, J. Sang, and H. Schuh, Multipath extraction and mitigation for high-rate multi-GNSS precise point positioning, *Journal of Geodesy*, *93*(10), 2037–2051, doi:10.1007/s00190-019-01300-7, 2019.

Zumberge, J. F., M. B. Heflin, D. C. Jefferson, M. M. Watkins, and F. H. Webb, Precise point positioning for the efficient and robust analysis of GPS data from large networks, *Journal of Geophysical Research: Solid Earth*, *102*(B3), 5005–5017, doi:10.1029/96JB03860, 1997.